Chapter 2
Characterization Methodologies of Optical Waveguides

Abstract The characterization of optical waveguides is a very important and essential step in any waveguide design and fabrication process. It is necessary to evaluate and confirm that the fabricated waveguide exhibits characteristics as designed. During materials selection and waveguide design, accurate measurements of key characteristics should be done with suitable methods. The major characteristics may include refractive index, layer thickness, optical coupling, optical loss, and nonlinear properties. Experimental evaluation and validation are necessary since these characteristics are rather difficult to determine theoretically. Such measurements provide important fundamental data to evaluate whether the waveguide is appropriate for integrated optical interconnection system, and use to specify the reason for the characteristics degradation. Therefore, the evaluation of the waveguide characteristics serves as a feedback to the design and the fabrication process, which is crucial for the modification and optimization of the waveguide performance. In this chapter, a series of optical waveguide characterization techniques will be elaborated.

2.1 Geometrical Inspection

Optical waveguides are structures that confine and direct optical signals in a region of higher effective index than its surrounding media. Beside the index difference providing the guiding region, the structure and the thickness of the fabricated waveguide plays an important role to confine the light. The minimum surface roughness and the side wall roughness give the minimum scattering loss. The light is no longer confined in the guiding layer and it begins to leak into the substrate if the thickness of the waveguide below the cutoff thickness. The thickness of the guiding layer also determines the guiding modes in the waveguide (Gang 2005). Optical specifications have been utilized throughout the design and manufacturing of a waveguide component or interconnect system to characterize how well it meets certain dimension performance requirements.

X.C. Tong, *Advanced Materials for Integrated Optical Waveguides*, Springer Series in Advanced Microelectronics 46, DOI 10.1007/978-3-319-01550-7_2,

Since the waveguides in optical integrated circuits have typical dimensions of only a few microns, observation of the waveguide across a given dimension cannot be accomplished without some equipment which featuring at least ×1,000 magnification. The waveguides are usually inspected under high power microscope to inspect the plan view (2-D) of the waveguide. With the 2-D view, the etching quality in the fabrication process, jagged at the edges, and particles dropped in the coating film can be observed clearly. Jagged and particles and some other surface quality issues can cause significant scattering loss in the waveguides (Gang 2005).

The surface quality of an optical surface describes its cosmetic appearance and includes such defects as scratches and pits, or digs. In most cases, these surface defects are purely cosmetic and do not significantly affect system performance, though, they can cause a small loss in system throughput and a small increase in scattered light. Certain surfaces, however, are more sensitive to these effects such as (Edmund 2013): (1) surfaces at image planes because these defects are in focus or on refractive surface and (2) surfaces that see high power levels because these defects can cause increased absorption of energy and damage the optic. The scratch designation is determined by comparing the scratches on a surface to a set of standard scratches under controlled lighting conditions. Therefore the scratch designation does not describe the actual scratch itself, but rather compares it to a standardized scratch according to related optical specifications. The dig designation, however, does directly relate to the dig, or small pit in the surface. The dig designation is calculated at the diameter of the dig in microns divided by 10. Scratch-dig specifications of 80-50 are typically considered standard quality, 60-40 precision quality, and 20-10 high precision quality.

Surface flatness is a type of surface accuracy specification that measures the deviation of a flat surface such as that of a mirror, window, prism, or plano-lens. This deviation can be measured using an optical flat, which is a high quality, highly precise flat reference surface used to compare the flatness of a test piece. When the flat surface of the test optic is placed against the optical flat, fringes appear whose shape dictates the surface flatness of the optic under inspection. If the fringes are evenly spaced, straight, and parallel, then the optical surface under test is at least as flat as the reference optical flat. If the fringes are curved, the number of fringes between two imaginary lines, one tangent to the center of a fringe and one through the ends of that same fringe, indicate the flatness error. The deviations in flatness are often measured in values of waves (λ), which are multiples of the wavelength of the testing source. One fringe corresponds to ½ of a wave. Flatness with 1 of a wavelength λ is considered typical grade, ¼ of λ flatness is considered to be precision grade, and 1/20 of λ is considered high precision grade (Edmund 2013).

Power, a type of surface accuracy specification, applies to curved optical surfaces, or surfaces with power. It is tested in a fashion similar to flatness, in that a curved surface is compared against a reference surface with a highly calibrated radius of curvature. Using the same principle of interference caused by the air gaps between the two surfaces, the interferences pattern of fringes is used to describe the deviation of the test surface from the reference surface. A deviation from the reference piece will create a series of rings, known as Newton's Rings. The more rings are present, the larger the deviation. The number of dark or light rings, not the sum of both light and dark, corresponds to twice the number of waves of error (Edmund 2013).

Irregularity, a type of surface accuracy specification, describes how the shape of a surface deviates from the shape of a reference surface. It is obtained from the same measurement as power. Regularity refers to the sphericity of the circular fringes that are formed from the comparison of the test surface to the reference surface. When the power of a surface is more than 5 fringes, it is difficult to detect small irregularities of less than 1 fringe. Therefore it is common practice to specify surfaces with a ratio of power to irregularity of approximately 5:1 (Edmund 2013).

The thickness and the topography of the waveguide can be measured using the surface profiler. Normally, surface profiling can be done using scanning electron microscope (SEM) or DEKTEK stylus surface profiler. SEM is a destructive method to analysis surface morphology. Stylus of the DEKTEK surface profiler could scratch the waveguide during its scanning on the sample. A noncontact optical surface profiler had been used for the surface profiling and topography (3-D), with white light interferometry. Film thickness, waveguide width, and the surface roughness of the coating can be measured using the surface profiler.

Surface roughness or surface finish measures small scale irregularities on a surface. They are usually an unfortunate by-product of the polishing process. Rough surfaces tend to wear faster than smooth surfaces and may not be suitable for some applications, especially those with lasers or intense heat, due to possible nucleation sites that can appear in small cracks or imperfections. Manufacturing tolerances of surface finish range from 50 Å RMS for typical quality, 20 Å RMS for precision quality, and 5 Å RMS for high quality (Edmund 2013).

2.2 Refractive Index Measurements

The refractive index is one of the most important properties of an optical waveguide. The refractive index profile has been used to calculate waveguide properties such as insertion losses, and cutoff wavelengths for propagating modes and the intensity distribution of the modes themselves. The refractive index can be modified to minimize losses, to yield a specific cutoff wavelength and to optimize the mode profile. Therefore, with a more accurate refractive index measurement, a more precise calculation of the waveguide properties can be obtained.

Several techniques have been used for the measurement of the refractive index distribution of waveguides, including reflectometry and ellipsometry, surface plasmon resonance (SPR), incoherent light transmission, the refracted near-field (RNF) technique, prism coupling, as well as the propagation-mode near-field method. The former three techniques have limited resolution and require the index enhanced region to be at or near the substrate surface. Ellipsometry and prism coupling are complimentary techniques for measuring the refractive indices of thin films. The RNF technique and the propagation-mode near-field method is another pair of complimentary techniques for measuring the refractive index profiles of optical waveguides (Chien 2004).

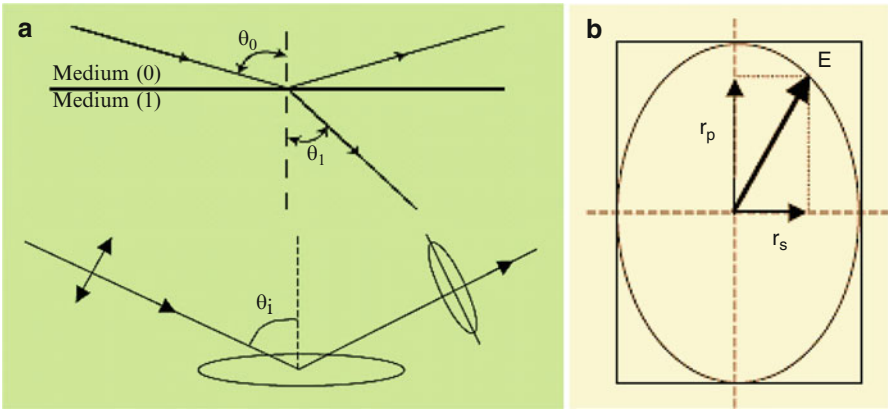

Fig. 2.1 Reflection and transmission of an incident light wave at a surface boundary (Elton 2007): (**a**) linearly polarized light reflected from a surface becomes elliptically polarized; (**b**) in plane polarized light, r_p and r_s oscillate in phase. In elliptically polarized light, there is a phase lag (Δ) between them, such that the electric field rotates and changes amplitude in time describing an ellipse

2.2.1 Reflectometry and Ellipsometry

Refractive index (n) is a complex number comprising a real refractive index and an imaginary part: the absorption (or extinction) coefficient. It may generally written as (Elton 2007)

$$n = n' - n'' \tag{2.1}$$

where n' is the real refractive index and n'' the extinction (absorption) coefficient. The real part of the refractive index describes how the speed of light changes as it enters the material. The extinction coefficient describes how light is absorbed (or scattered). In a transparent material, absorption is zero and $n = n'$. The reflectivity of an absorbing material depends on both parts of the complex refractive index, and, in fact a highly absorbing material will in general be much more reflective than a corresponding transparent material. This is why metals, for instance, make such good mirrors—the refractive index of aluminum is 1.21–6.92 (Elton 2007).

Reflectometry generally yields an approximation to the real part of the refractive index. The well-established technique of ellipsometry, by contrast, can determine both the real refractive index and the extinction coefficient. As shown in Fig. 2.1, linearly polarized light can be thought of as having two perpendicular electric field components, denoted r_p and r_s, oscillating in phase. When linearly polarized light is reflected from a surface, in general the amplitudes r_p and r_s change and so does the phase between them. The light becomes elliptically polarized. If the substrate is

non-absorbing, the phase change is zero and linear polarization is preserved. Ellipsometry is well-established experimental method for analyzing the phase and amplitude of reflected polarized light in order to extract information about the surface. Various types of ellipsometers have been built up, but a common form is the rotating polarizer. In this design, linearly polarized light is incident on the sample surface, as illustrated in Fig. 2.1a, but the polarizer is rotated, so that the plane of polarization rotates about the axis of the incident light. On the detector side, the (generally) elliptically polarized light is passed through a fixed analyzer. The intensity of light on the detector oscillates with rotation of the incident polarizer according to the amplitude and phase change at the specimen. The fundamental equation of ellipsometry can be expressed as (Elton 2007)

$$\rho_e = \tan \Psi e^{\Delta} \tag{2.2}$$

$$\Psi = |R_p|/|R_s| \tag{2.3}$$

where Δ is the phase change between r_p and r_s upon reflection, Ψ is the angle whose tangent is the ratio of the intensity of the R_p and R_s components. In the case of reflection from a simple substrate, Ψ and Δ can be inverted directly to give the real refractive index and extinction coefficient. In any other situation, e.g., in the presence of one or more thin films, surface roughness, interface roughness, it is necessary to start from a model of the surface and to fit the measured values of Ψ and Δ to the model to obtain a best fit. For a non-absorbing substrate, $\Delta = 0$, and ρ_e is real. But in general, if absorption is present, ρ_e is a complex number.

With these parameters, the complex refractive index of the sample (thin film of optical waveguide) can be calculated as (Jung et al. 2004)

$$\widetilde{n}_1 = \frac{\left[\sqrt{1 - 4\sin^2(\theta_0)\tan(\Psi)e^{j\Delta} + 2\tan(\Psi)e^{j\Delta}\tan^2(\Psi)e^{j\Delta}}\right]\widetilde{n}_0 \sin(\theta_0)}{\cos(\theta_0)[1 + \tan(\Psi)e^{j\Delta}]} \tag{2.4}$$

where n_0 is the complex reflective index of the ambient. θ_0 is the angle of incidence. The data from the ellipsometer are values of Ψ and Δ as a function of wavelength. Using (2.4), these data can be used to calculate the complex index of refraction as a function of wavelength.

In the reflectometry measurement, the sample surface is illuminated with s- and p-polarized light. The reflected intensities R_p and R_s of the p and s polarized components are measured, and are used to calculate a refractive index using the form of the Fresnel equations for a transparent substrate (Elton 2007):

$$n_R = \sin\theta_i \sqrt{1 + \left(\frac{1-\rho}{1+\rho}\right)^2 \tan^2\theta_i} \tag{2.5}$$

where $\rho = \sqrt{R_p/R_s}$. The reflectometry analysis assumes that the material is non-absorbing. If the material truly is non-absorbing, then reflectometry will return the correct real refractive index. If the material is absorbing, then reflectometry will

return an approximation to the real refractive index. This approach is a trade-off between absolute accuracy for refractive index on one hand and a desire for speed of operation and the ability to measure several other parameters (such as roughness) at the same time. For the types of material that reflectometry is aimed at, the simplified measurement of refractive index generally works very well. However, if the surface is rough, the reflected light will be scattered over a range of angles making the analysis extremely difficult.

Comparably, ellipsometry and reflectometry are closely related techniques with rather different aims. Ellipsometers are normally used for the analysis of very smooth substrates, thin films, adsorption processes, or layer growth for optical waveguides. With a suitable model of the surface, ellipsometry is a powerful technique for obtaining information on refractive index, extinction, and film thickness. Ellipsometry can be applied successfully to relatively rough surfaces, but measurement times can be fairly long. The reflectometer is generally designed specifically for determining an approximate real refractive index, which is typically accurate to about 0.01 which is probably of the same order as systematic instrumental errors due to alignment and calibration. The reflectometer can also be used to measure macroroughness, microroughness, and various gloss values. The approximations in the determination of refractive index mean the reflectometer cannot provide meaningful refractive index or microroughness results for metals or thin transparent films, although macroroughness and gloss are still valid. Both techniques have merits and limitations: although closely related, they do not ultimately do the same. If a choice is needed between the two methods, it must depend on the end applications.

Compared with prism coupling, ellipsometry and prism coupling are complementary techniques that can both be used to measure the index of bulk materials and to simultaneously measure film thickness and refractive index. In general, ellipsometry is ideal for measuring thin films such as gate oxides, pyrolytic silicon nitride, or any film whose thickness is thinner than a few thousand angstroms. For the measurement of thicker samples, the prism coupler is superior. In addition, ellipsometry requires accurate advance knowledge of the real and imaginary parts of the substrate refractive index. If these parameters are not known, or if they vary due to roughness or other surface conditions, appreciable errors can result. The prism coupling technique is only weakly sensitive to substrate optical parameters. In the case of a film over a lower index substrate, thickness and index as measured by prism coupling are weakly dependent on the real part of the substrate index only. The prism coupler can also be used to measure the bulk refractive index of the substrate directly (Chien 2004).

2.2.2 Surface Plasmon Resonance

SPR reflectivity measurement can be used to characterize thickness and index of refraction of ultra-thin films covering on surface of noble metal (Au, Ag). Plasmon is a strongly attenuated electromagnetic wave propagating along the boundary between

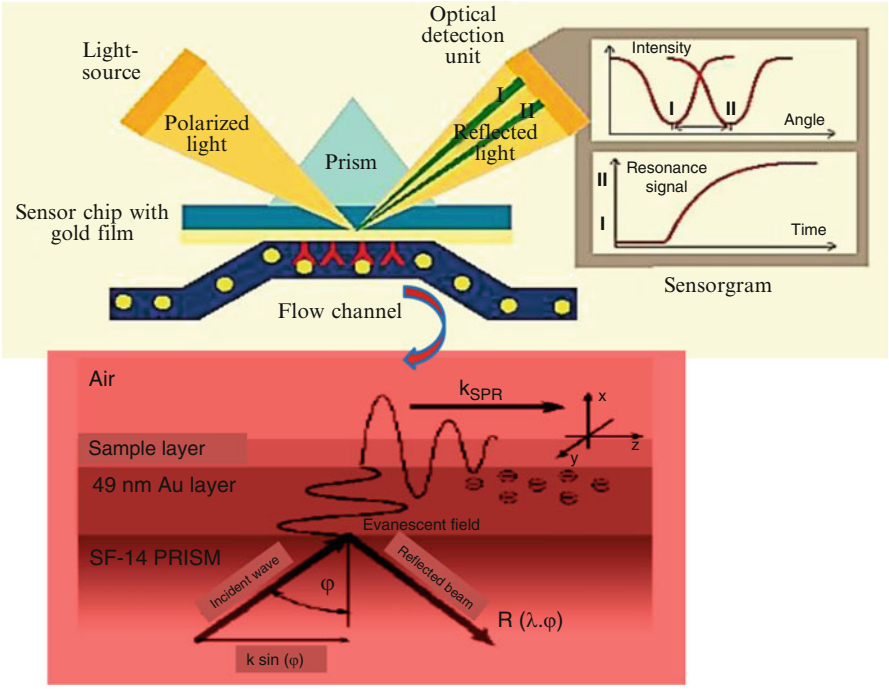

Fig. 2.2 The schematic of SPR measurement setup

the thin metal layer and the dielectric one above it, as shown in Fig. 2.2. The energy of the incident wave coupled with the surface plasmon is irrevocably dissipated in the system, so it cannot appear in the wave reflected from the metal/dielectric interface. For the plasmon resonance in the prism configuration, SPR excitation by the incident light wave at the base of the prism occurs when the wave vector of the plasmon k_{SPR} and the projection of the incident wave vector k in the direction of propagation of the plasmon are equal. The refractive index of the dielectric film can be calculated with the following equation (Tyszkieiwcz et al. 2005):

$$k \sin \varphi = k_{SPR} \tag{2.6a}$$

$$k_0 n_{prism} \sin \varphi_i = k_0 \sqrt{\frac{\varepsilon_{Au} n_s^2}{\varepsilon_{Au} + n_s^2}} \tag{2.6b}$$

where k_0 is wave vector of light in a vacuum, k_{SPR} is wave vector of the surface plasmon, n_s is a refraction index of the dielectric film above the metal layer, ε_{Au} is a real part of the dielectric complex constant of the active plasmon layer (e.g., Au), n_{prism} is a refraction index of the prism, and φ_i is an incident angle of light against the normal to the prism base.

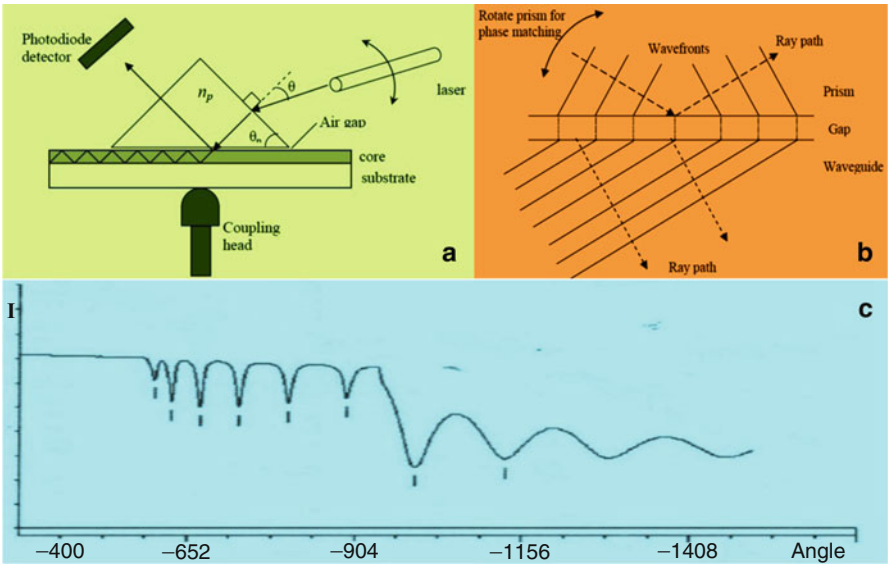

Fig. 2.3 Schematic illustration of prism coupling technique for the measurement of the refractive index and the thickness of thin films, which utilizes a high-index prism to excite a guided wave through phase matching between the incident wave and guided mode (Gang 2005): (**a**) prism coupling assembly; (**b**) phase-matching condition at prism–waveguide interface; (**c**) rotation spectra against angle of incidence θ of the prism

2.2.3 Prism Coupling

The prism coupling technique has been used for the measurement of the refractive index n and the thickness t of thin films, which utilizes a high-index prism to excite a guided wave through phase matching between the incident wave and guided mode. A prism which having the refractive index, n_p, higher than the refractive index of the measured material was clamped onto the film and the substrate was supported against a coupling head. The clamp created a small pressure to ensure the prism interface close to the right angle corner of the prism. This produces a small air wedge which is required to achieve efficient launching of light into modes in the film. A He–Ne laser (visible light) was used for 633 nm measurements. The laser beam was launched onto the diagonal prism face. The whole assembly was then rotated about a vertical axis until a guided mode was launched into the film (Fig. 2.3a). The effective index of the light wave along the bottom surface of the prism is adjusted to match that of a waveguide mode (Fig. 2.3b). The mode intensity was optimized by movement of the laser beam in the vertical direction. The prism was rotated until the beam was reflected back along the normal and the angular position for this was noted. This was the reference position against which the mode angles were measured. Rotating the sample and detector yields the rotation spectrum

of the references against the angle of incidence, θ, at the prism as shown in Fig. 2.3c. Each sharp dip in the spectrum indicates a mode in the slab waveguide. The software of the equipment solved the relevant (2.7) and (2.8) to give the value of the refractive index and film thickness. The measured angles for the first and second modes are used to calculate the effective index for each TE mode in the film using the equation (Gang 2005)

$$n_{\mathrm{eff}(m)} = n_{\mathrm{p}} \sin\left(\theta_{\mathrm{p}} + \sin^{-1}\left(\frac{\sin\theta}{n_{\mathrm{p}}}\right)\right) \tag{2.7}$$

where n_{p} is the prism index, θ_{p} is the prism angle, and θ is the measured incident angle for mode $m = 0, 1, \ldots$. In order to calculate the bulk index for the film from the effective indices it is necessary to solve the resonance equation for mode propagation in the film (Gang 2005)

$$k_0 t(\varepsilon_0 - \varepsilon_{\mathrm{m}})^{1/2} = \tan^{-1}\left[\frac{(\varepsilon_{\mathrm{m}} - \varepsilon_{\mathrm{s}})}{(\varepsilon_0 - \varepsilon_{\mathrm{m}})}\right]^{1/2} + \tan^{-1}\left[\frac{(\varepsilon_{\mathrm{m}} - \varepsilon_{\mathrm{a}})}{(\varepsilon_0 - \varepsilon_{\mathrm{m}})}\right]^{1/2} + m\pi \tag{2.8}$$

where k_0 is the free-space wave vector and the permittivities of the materials are ε_0 for the film, ε_{a} for air, ε_{s} for the substrate, and ε_{m} for the modal effective index. t is the film thickness. The equation is solved by an iterative method.

However, the following factors limit the utilization of the prism coupling technique (Chien 2004):

(a) The film must be thick enough to permit the propagation of at least two modes. If only one mode is observed, the prism coupler may still be used to determine one of the parameters n and t if the other is known from an independent measurement.
(b) The method is a contact method and it is necessary to press the film against the base of the prism. Extra care must be taken when measuring polymers. In general, the technique is nondestructive.
(c) Alignment of small samples with the coupling spot requires a certain degree of skill and experience. Typically, the laser spot is collimated to approximately 1.0 mm^2 and this can be a challenge where the proton beam written samples are only about 2.0 $\times$ 2.0 mm^2 in size.

2.2.4 *Propagation-Mode Near-Field Technique*

Propagation-mode near-field method, also known as the scalar wave inversion technique, is a nondestructive technique which estimates the refractive index distribution in a waveguide from its mode field intensity by an inversion of the scalar wave equation. One of the advantages of the technique is that it requires no prior knowledge of the shape of the refractive index and does not require the waveguide to possess any form of cross sectional symmetry. However, the main

limitations of the technique are (a) the waveguide has to be weakly waveguiding; and (b) only the fundamental mode of the propagation is excited. For a weakly guiding waveguide, where the peak refractive index change is small, the optical field strength of the fundamental mode of excitation, $\Psi(x, y)$, and refractive index $n(x, y)$ relationship may be described by the scalar wave equation (Chien 2004):

$$n^2(x,y) = \left(\frac{\beta}{\kappa_0}\right)^2 - \frac{\nabla_T^2 \Psi(x,y)}{\kappa_0^2 \Psi(x,y)} \tag{2.9}$$

where $\nabla_T = \frac{\partial}{\partial x} + \frac{\partial}{\partial y}$ and k_0 is the free-space wave number; $n(x, y)$ is the refractive index and β is the propagation constant. Substituting $I(x, y) = \Psi^2(x, y)$ for the intensity and introducing $n(x, y) = n_B + \Delta n(x, y)$ (where $\Delta n(x, y)$ is small), (2.9) becomes:

$$\Delta n(x,y) = \frac{\beta^2}{2n_B k_0^2} - \frac{n_B}{2} - \frac{\nabla_T^2 \sqrt{I(x,y)}}{2n_B k_0^2 \sqrt{I(x,y)}} \tag{2.10}$$

where n_B is the substrate refractive index and, β/k_0 is the effective index, N_{eff}. These two terms on the right hand side are unknown constants. Hence, the fundamental mode field intensity $I(x, y)$ can be used to uniquely determine the refractive index distribution of the waveguide to within an arbitrary constant. This constant can be found by matching the refractive index away from the waveguide core to that of the substrate. In the weak guidance approximation, Δn is small and $n_B \approx \frac{\beta}{k_0} = N_{eff}$. Hence (2.10) can be approximated to

$$\Delta n(x,y) = -\frac{\nabla_T^2 \sqrt{I(x,y)}}{2n_B k_0^2 \sqrt{I(x,y)}} \tag{2.11}$$

The substitution of $\Psi(x,y) = \sqrt{I(x,y)}$ is based on the assumption that there is no phase variation across the measured wave field. Such an approximation is valid since the mode field intensity is measured at the waveguide end face where the phase variation is negligible. Due to the second-order derivatives involved in (2.11), good mode profile data that is precisely focused on the CCD array is essential to obtaining accurate refractive index profiles. Multiple images of the near-field mode profiles of the waveguides must be taken and averaged in time (Chien 2004).

2.2.5 *Refracted Near-Field Technique*

A typical setup for the RNF technique is given in Fig. 2.4 (Goering and Rothhardt 1986). The setup is applicable to both planar or channel waveguides. Collimated light is focused into the end face of the waveguide using a microscope objective. The substrate is placed with the waveguide downwards onto the glass block, with a

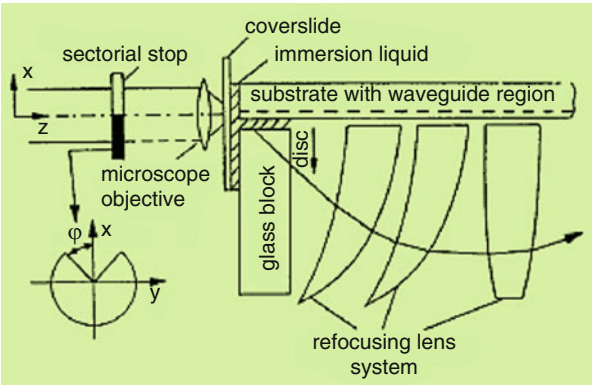

Fig. 2.4 Schematic experimental setup for the refracted near-field method (Goering and Rothhardt 1986)

film of immersion liquid film between them. Light escaping from the back surface of the glass block and passing the aperture stop (disk) is refocused by a system of hemilenses onto a large area photodiode. The detected signal is inversely proportional to the refractive index changes encountered at the waveguide end face during a scan across the sample. From the known refractive index values of the immersion liquid and the glass block, the waveguide's refractive index distribution can be determined using a linear interpolation. The experimental setup for the RNF technique is considerably more complicated compared to that for the propagation-mode near-field method. Apart from these hardware issues, there are several issues pertaining to the linearity between the measured RNF signal and the refractive index of the focal point; and the issues relating to the accuracy of RNF measurements due to the uncertainty of the calibration of the refractive indices of the immersion oil and the reference blocks. On the other hand, the setup for the propagation-mode near-field method can be readily acquired from off-the-shelves components, without the need for any custom build components; while yielding the same information on the refractive index distribution. One advantage of the RNF technique over the propagation-mode near-field method is its ability to measure the refractive index distributions of multi-mode waveguides (Chien 2004).

2.2.6 M-Line Spectroscopy (MLS)

MLS is one of the most accurate methods to determine optogeometric parameters including refractive index and film thickness of waveguiding films. It allows an evaluation of a refractive index with accuracy up to 10^{-4}. The accuracy of film thickness measurement is also as high as 10^{-2}–10^{-3} (Wu 2005). MLS also uses the same principle concept as prism coupling, and is particularly well adapted to the accurate determination of the film refractive index and thickness. In comparison with other methods, MLS has important advantages such as the requirement of only angle measurements, the opportunity to determine the anisotropy of the layer and the fact that this is a nondestructive method. The disadvantages of MLS, however,

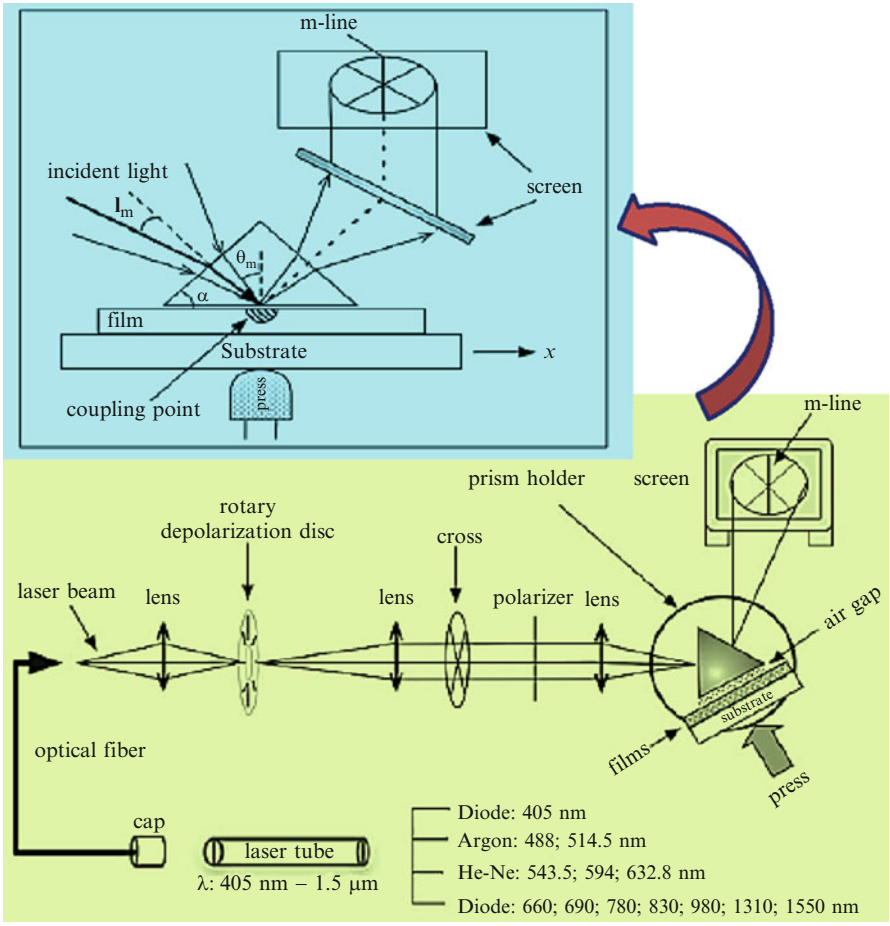

Fig. 2.5 Schematic illustration of the prism coupling technique used in MLS (Wu 2005)

include (a) the film must be thick enough to support at least two guided modes, (b) the substrate used has to be transparent at the required wavelength, (c) the layer must be hard enough to be pressed against the base of a prism and the roughness of the film must be as low as possible to increase the accuracy. Also the observation of the m-dark lines requires a certain degree of skill and experience and only an absorption up to 80 dB/cm in the direction of propagation is tolerable (although at these levels it will reduce the accuracy of the measurements).

Usually, MLS uses only one wavelength (the most popular is 632.8 nm, He–Ne laser) and the calculation is carried out on the premise of step-index model. A way to confirm the step-index assumption is to conduct MLS measurements at various wavelengths in order to verify whether the sample thickness is wavelength dependent or not. For such application, a multi-wavelength MLS (MWMLS) has been developed. The schematics of MLS and MWMLS are shown in Fig. 2.5. The refractive index (n_f) and thickness (T) of the thin film can be calculated using the step-index model (Wu 2005):

When using TE polarization

$$\frac{T}{\lambda}=\frac{1}{2\pi\sqrt{\left(n_{\mathrm{f}}^2-N_m^2\right)}}\left[m\pi+\tan^{-1}\left(\frac{\sqrt{\left(n_0^2-N_m^2\right)}}{\sqrt{\left(N_m^2-n_{\mathrm{f}}^2\right)}}\right)+\tan^{-1}\left(\frac{\sqrt{\left(n_{\mathrm{s}}^2-N_m^2\right)}}{\sqrt{\left(N_m^2-n_{\mathrm{f}}^2\right)}}\right)\right] \tag{2.12}$$

When using TM polarization

$$\frac{T}{\lambda}=\frac{1}{2\pi\sqrt{\left(n_{\mathrm{f}}^2-N_m^2\right)}}\left[m\pi+\tan^{-1}\left(\frac{n_{\mathrm{f}}^2}{n_{\mathrm{c}}^2}\frac{\sqrt{\left(n_0^2-N_m^2\right)}}{\sqrt{\left(N_m^2-n_{\mathrm{f}}^2\right)}}\right)+\tan^{-1}\left(\frac{n_{\mathrm{f}}^2}{n_{\mathrm{s}}^2}\frac{\sqrt{\left(n_{\mathrm{s}}^2-N_m^2\right)}}{\sqrt{\left(N_m^2-n_{\mathrm{f}}^2\right)}}\right)\right] \tag{2.13}$$

where $N_m=n_{\mathrm{p}}\sin\left(\alpha+\arcsin\left(\frac{\sin i_m}{n_{\mathrm{p}}}\right)\right)$.

All the parameters are known or can be measured separately. If the film is thick enough to support more than two modes on the same polarization, the method becomes a self-consistent one because the two unknown n (refractive index) and T (thickness) can be determined from more than two independent measurements. The values of n_{f} and T is just a computational problem in order to adjust these values until theoretical values of N_m are close to the experimental values of N_m. If the agreement between experimental and calculated values of N_m is in the range of 0.001 or less, the step-index model is satisfied. If the step-index model is not satisfied, the refractive index profile versus the sample thickness can be reconstructed using inverse Wentzel–Kramer–Brillouin (WKB) method which provides reliable and quick result in the case of slight refractive index variation (Wu 2005). However, at least four observable modes are required or such a calculation and a judicious choice of the exciting wavelength are necessary.

MWMLS allows studying a bulk material such as the substrate and its dispersion curve. For this latter application, just a face of the material must be polished, or bulk sol–gel must be elaborated in a very flat and smooth polymer box.

2.3 Coupling Techniques

For an integrated optical waveguide system, before exciting guided-mode propagation, introducing an incident light into the waveguide or transmitting the light out of the waveguide to the receiver is an important step because the laser beam belongs to a radiation mode which cannot propagate directly in the waveguides. Therefore, it is necessary to find a technique to effectively confine and couple the laser beam with the waveguide. Several techniques have been used for carrying out such coupling requirements, including prism coupling, end coupling, tapered and/or

Table 2.1 Comparison of some light wave coupling techniques (Christensen et al. 1992)

Techniques	Advantages	Disadvantages
Prism coupling	High efficiency; mode selective	Complex; difficult to align
End coupling	High efficiency for thick waveguides	Difficult to align for thin waveguides
Launch coupler	Tolerant of alignment	Long, thin taper required for thin waveguides
Grating coupler	Tolerant of alignment; mode selective	Lower efficiency

lunch coupling, and grating coupling. Prism coupling and end coupling are the most extensively used methods. Prism coupling is highly efficient and is mode selective, but requires placement of a prism on top of the waveguide with a carefully adjusted gap between the prism and the waveguide. This makes the prism coupling technique unsuitable for fast, alignment tolerant coupling to a disposable waveguide system. End coupling is simple and efficient, but the input beam from the source needs to be directed into the end of waveguide, requiring alignment accuracy at least as small as the thickness of the guide. For thin waveguides this may be a difficult requirement, especially if the waveguides are replaceable. The non-tapered launch coupler works well for thick waveguides (thicknesses greater than about 1 mm) and is simple in design, but its coupling efficiency drops for thinner guides. The tapered launch coupler gives better efficiency for the thinner waveguides, but fabricating the tapered end is more difficult and makes the coupler end more fragile. The grating coupler is relatively easy to fabricate once the proper release agent is determined and the molding steps work out. The coupling efficiency of the grating coupler is not as high as the launch coupler, probably due to imperfections in the replication process. The grating coupler is mode selective however, and would be a better choice than the launch coupler for a thin film, few-mode guide. The advantage and disadvantage of some coupling methods are summarized in Table 2.1 (Christensen et al. 1992).

2.3.1 Prism Coupling Method

The prism coupling method uses a high-index prism to excite an incident wave to a guided mode. As shown in Fig. 2.6, a prism with a refractive index n_p is put close to the waveguide with a thin gap layer of air (index $= n_c = 1$) between them. When the light beam is launched into the bottom of the prism at an angle θ, the propagation constant of prism β along the waveguide plan (the z-direction) is given as (Wu 2005):

$$\beta_p = k_0 n_p \sin\theta \tag{2.14}$$

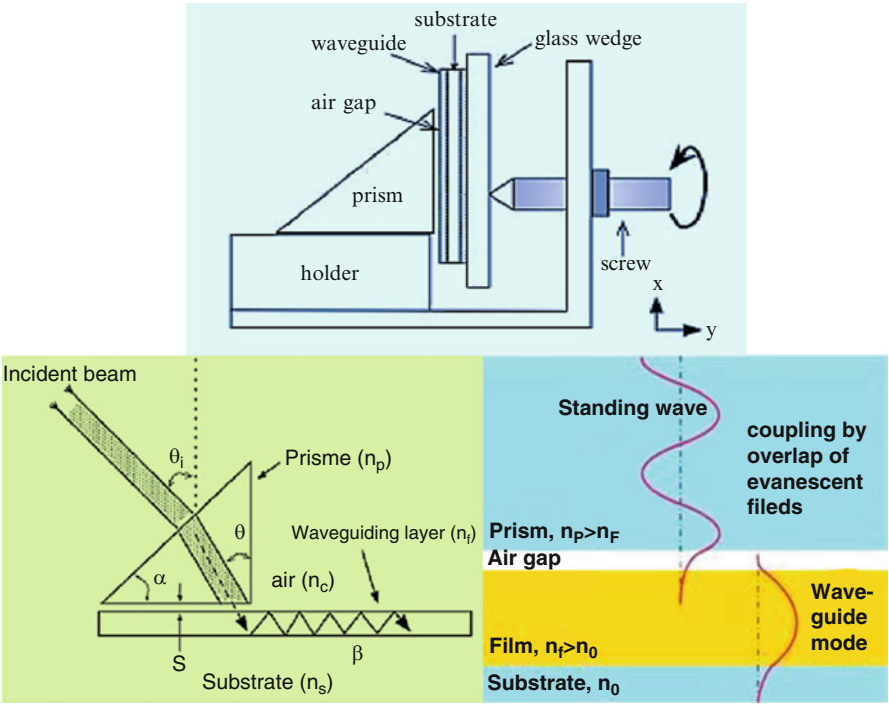

Fig. 2.6 Schematic illustration of prism coupling method uses a high-index prism to excite an incident wave to a guided mode

According to Snell's law, the incident light angle θ_i is related to the angle in the prism by

$$n_c \sin(\theta_i - \alpha) = n_p \sin(\theta - \alpha) \tag{2.15}$$

where α denotes the angle of the prism and n_p is the index of the prism. If there is no waveguide under the prism, the beam of the incident angle θ satisfying $n_p \sin\theta > n_c$ is entirely reflected at the bottom of the prism and penetrates as an evanescent wave into the air gap. When β_p adjusted by θ is consistent with the propagation constant of a guided mode β_f, the guided wave is excited through the distributed coupling resulting from phase matching between the evanescent wave and the guided mode. This condition is called matching phase. This energy transfer is effectuated through the evanescent wave created in the intermediate air gap between prism and waveguide, which is called the optical tunneling effect. Under the condition of matching phase, the effective refraction index of mth mode, N_m can be expressed as (Wu 2005)

$$N_m = n_w \sin\theta_m = n_p \sin\theta \tag{2.16}$$

Combined (2.15) and (2.16), N_m can be rewritten as (Wu 2005):

$$N_m = n_p \sin\left(\alpha + \arcsin\left(\frac{\sin\theta_i}{n_p}\right)\right) \tag{2.17}$$

Thus a value for the effective refractive index of each mode can be obtained since the values of n_p and α are known and θ_i can be directly measured. In addition, the propagation constants can be inferred since $\beta_m = k_0 \cdot N_m$. Once the values of β for two modes, β_m and β_{m+1}, can be calculated, the refractive n_w, and the thickness d of the waveguide can be inferred with (2.13).

In practice, the air gap thickness (S) plays an important role in prism coupling method. In order to create the optical tunneling effect, S has to be optimized. If the thickness is too large the evanescent wave is attenuated before being able to excite the guided mode of waveguide. Conversely, a too narrow air thickness provokes an angular displacement of the guided mode so the evanescent wave cannot correctly transmit into the waveguide. These facts mean that a careful adjustment of S is required. In order to effectuate an energy transfer by the prism coupling method, three conditions must be met (Wu 2005): (a) the laser beam must have the same polarization as the excited mode; (b) the thickness of the air gap S has to be carefully controlled in the range around 100 nm; and (c) the incident light has to be in accordance with the matching phase.

The prism coupling method is particularly adapted for the planar waveguide. The implied surface of the prism has to be well polished and of good quality. The major advantages of this method include: non-destructive, and allows changing the position of the coupling point around the sample; easy manipulation and high efficiency, about 80 % for input and output couplings; ability to selectively excite any guided modes by adjusting the angle of the incident light.

2.3.2 *End-Coupling Method*

The end-coupling technique is the simplest method to excite a guided wave. A light wave with a profile similar to guided mode is directly launched into an end-face normal to guided-wave propagation as shown in Fig. 2.7 (Wu 2005). The light is focused into one end of the waveguide using a microscope objective lens, and propagates along the whole length to emerge as a highly divergent beam from the opposite end. The general procedure is to image the output onto a screen using a second objective lens. For planar waveguides a very bright horizontal line should be observed on the screen under correct launch conditions.

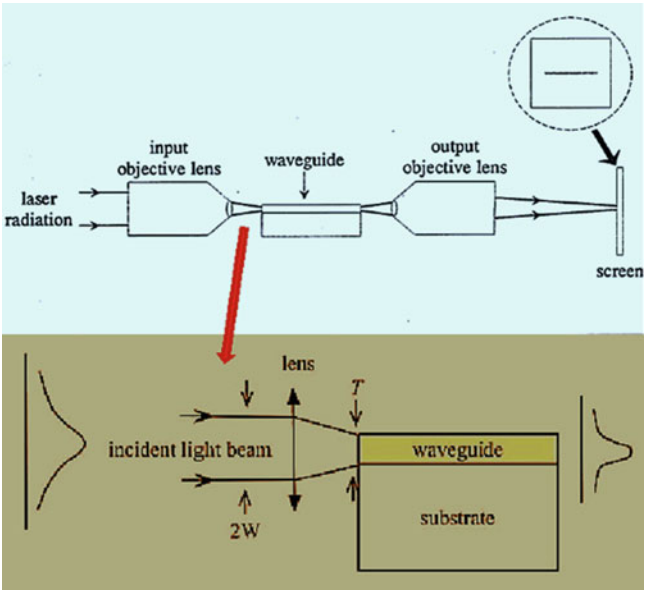

Fig. 2.7 Schematic illustration of end-coupling technique

In order to obtain a high efficiency, the incident-wave profile must be as close as possible to the profile of the guided wave. The coupling end face must exhibit extremely high optical quality and defectless which can be prepared by polishing, or cleaving treatments. End-face flatness and the alignment accuracy are strictly required. The main disadvantage of this method is that it excites all the guided modes simultaneously and it is not possible to select a particular excited mode when analyzing a multi-mode waveguide.

2.3.3 Lunch and Tapered-Coupling Method

The launch coupling basically uses a fixed lunch waveguide permanently to align with respect to the source beam to which a removable function waveguide is placed in contact. The input beam may be coupled from the source to this launch waveguide by any means: end coupling, grating coupling, or even prism coupling. The function waveguide is then placed on top of the launch coupler and light is coupled into the function guide by simple propagation. Coupling gel (or more permanent coupling polymer) can be used to increase the index match between the two guides. This scheme allows for great latitude in the placement of the

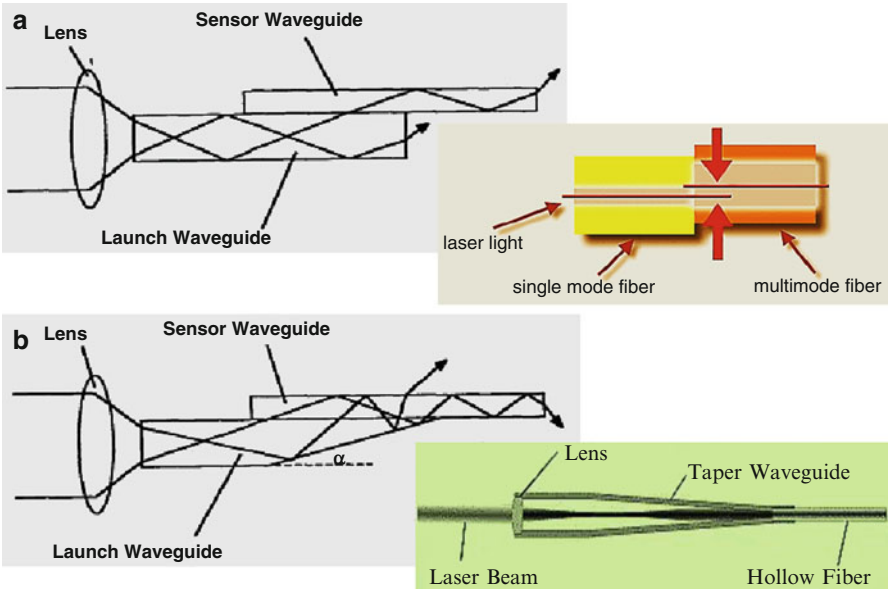

Fig. 2.8 Schematic illustration of launch coupler with another waveguide such as sensor waveguide placed on top: (**a**) no-tapered and (**b**) tapered

function waveguide with respect to the coupler. Vertical alignment is achieved automatically by the mating surfaces, and longitudinal positioning of the function waveguide is not critical (assuming an overlap distance of at least a few waveguide thicknesses). Figure 2.8 shows two versions of the launch coupler with a function waveguide in place. The first version, shown in Fig. 2.8a, uses a non-tapered launch guide. Ray theory predicts that the percentage of light initially in the launch guide that is coupled into the sensor is dependent on the ratio of the thicknesses of the two guides in the following manner (Christensen et al. 1992):

$$\% \text{ Coupling} = t_s/(t_s + t_j) \tag{2.18}$$

where t_s is the thickness of the function waveguide and t_j is the thickness of the launch waveguide. Thus, when the two guides have the same thickness, the coupling efficiency is 50 %. When the function waveguide is much thinner than the launch guide, however, the coupling efficiency drops considerably.

For thin function waveguides, the tapered version of the coupler as shown in Fig. 2.8b, gives higher efficiency. The design is based upon the concept of transforming narrow-angle/broad-area illumination in the launch waveguide (as initially coupled in from a laser source) into broad-angle/narrow-area light in the sensor waveguide. For small taper angles, the coupling efficiency can be quite large.

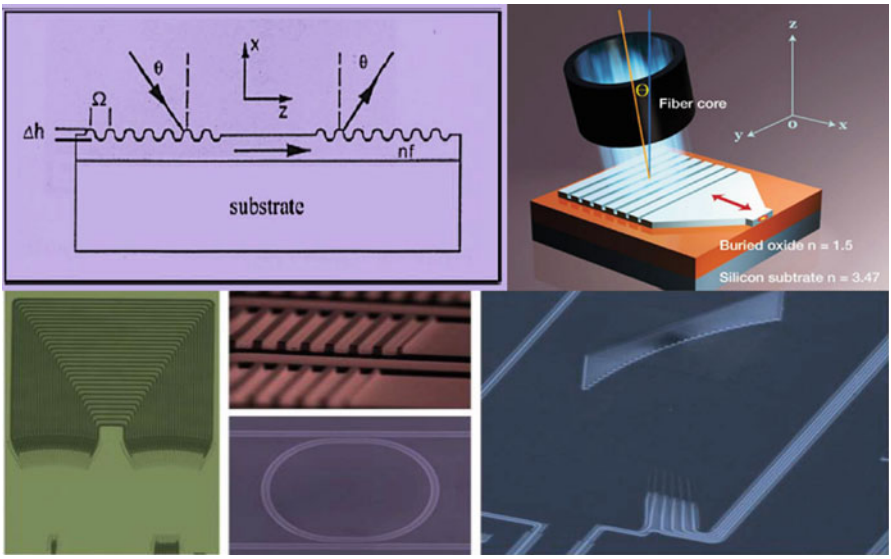

Fig. 2.9 Schematic illustration of grating coupling method and examples of some grating couplers

The tapered-coupling usually consists of tapering the end of the waveguide by a bevel length from 10 to 100 times the operating wavelength. This method is favored for high-index waveguides, such as GaAs, which require an expensive high-index prism when using the prism coupling method. When the guided mode propagates inside the waveguide that exceeds the critical angle, the total internal reflection is alternated at the tapered part and gradually reaches the cutoff condition in the substrate. An optical fiber can be coupled at the output beam position and an input coupling is also possible by supplying a laser beam which is conjugate to the output beam. This method is able to selectively excite guided modes, and has no limitation for the refractive index of waveguide. However, this method is destructive, and it is not easy to taper a waveguide precisely so it is not used frequently for experimental analyses.

2.3.4 Grating Coupling Method

This technique relies on a periodic grating structure on the surface of the waveguide as shown in Fig. 2.9. When a laser beam with propagation vector β_0 is incident in the grating region, the light is diffused by the gratings. According to such diffraction, the wave components with the propagation vector $\beta_g = \beta_0 + \gamma K$ is produced, called space harmonics where γ is the order of diffraction and K is the grating vector correlated to

the fundamental period Ω by $K = 2\pi/\Omega$. When β_g equals to the propagation vector of guided mode, the incident light can be coupled into the waveguide. This condition is called matching phase condition which can be expressed as (Wu 2005):

$$\beta_g = \beta_0 + 2\pi\frac{\gamma}{\Omega} = k_0 N_m \tag{2.19}$$

$$N_m = n_c \sin\theta + \frac{\gamma\lambda_0}{\Omega} \tag{2.20}$$

The grating coupling method is permanent and allows selection of guided mode but the implement requires a certain degree of delicate skill. The coupling efficiency depends on the grating structure, such as grating period (Ω), grating depth (Δh). The grating coupler has showed moderate tolerance to alignment. However, the efficiency is somewhat sensitive to the lateral beam position on the grating for a focused input beam. The beam position had to be within approximately 1–2 mm of the end of the grating (toward the waveguiding region) to achieve the highest efficiency. If the beam was too far away from the grating end, light coupled into the guide would be coupled back out by the grating before reaching the guide, reducing the amount coupled.

2.4 Optical Loss

Light wave experiences attenuation or losses as it propagate through an optical waveguide. An expression for the amount of optical power remaining in the waveguide after propagating a distance x is given in the following expression (Chien 2004):

$$I(x) = I_0 10^{\left(-\frac{\alpha x}{10}\right)} \tag{2.21}$$

where I_0 is the initial power, $I(x)$ is the transmitted power through the waveguide at a distance x (cm), and α is defined as the attenuation coefficient of the waveguide, measured in decibels per centimeter (dB/cm). The loss, L in decibels (dB) is defined as (Chien 2004)

$$L(\mathrm{dB}) = -10\log\left(\frac{I(x)}{I_0}\right) \tag{2.22}$$

In order to make a waveguide into any functional optical devices, its propagation losses, or transmission losses must be kept as low as possible. Light propagation in optical waveguides can be affected by a certain number of distortions due to the random distributions of imperfections within the waveguides. Many factors are considered to disturb the light propagation and increase the propagation losses: (a) Radiation losses due to the guided mode converse to the radiation mode.

(b) Mode conversion losses due to conversion from the excited mode to other guided modes. Optical energy can be lost from the waveguides modes by the conversion from the excited mode to other guided modes. When a waveguide is simply used for light power transmission, mode conversion does not cause substantial loss. In a device where a guided mode performs a function, mode conversion is an important factor affecting performance. (c) Absorption losses due to light absorption in the waveguide materials. Optical energy is converted into phonon energy in the form of heat. The most important losses are inter-band absorption, impurity absorption, and carrier absorption, which could either be an inherent effect due to the impurities in the material or could be an induced absorption resulting from the fabrication process. (d) Diffusion losses or scattering losses due to the imperfection of the waveguide structure. Scattering at the waveguide interfaces could also be an inherent effect due to the defects or surface roughness existing in the original material or formed after the fabrication process. Scattering losses are due to the imperfections of the waveguide structure and the quality of the material used. Voids, contaminant atoms, crystalline defects within the volume of the waveguide cause volume scattering while surface scattering loss can be significant for rough (bumps and valleys) surfaces of the waveguide. (e) Tunneling losses that only occurs in barrier optical waveguides produced by ion modification. A guide confined by a narrow optical barrier would be very susceptible to such losses.

2.4.1 Propagation Losses by Radiation

The light radiation may take place when the propagation constant of the guided mode (β) is close to that of the substrate (β_s). When $\beta \gg \beta_s$, the distribution of the electromagnetic field can be concentrated in the film center as shown in Fig. 2.10a. Otherwise, the energy transfer by the guided mode is partially dispersed into the substrate or the upper cladding. Actually, this radiation loss occurs when the refractive index of the film is close to that of the substrate or when the film thickness is close to the cutoff thickness. It is also probably induced by the imperfection existing inside the waveguide which could change the wave propagation to radiation mode and dissipate the propagation power out of the waveguide. This distortion due to the imperfections is classified as a factor of propagation losses by diffusion (Wu 2005).

2.4.2 Propagation Losses by Absorption and Mode Conversion

The propagation losses by absorption are mainly due to the light absorption by the materials of waveguides. The optical absorption can result from the anionic deficit (e.g., oxygen), defects (stoichiometry), impurities which absorb the light and reduce the light intensity as illustrated in Fig. 2.10b. This mechanism of propagation losses

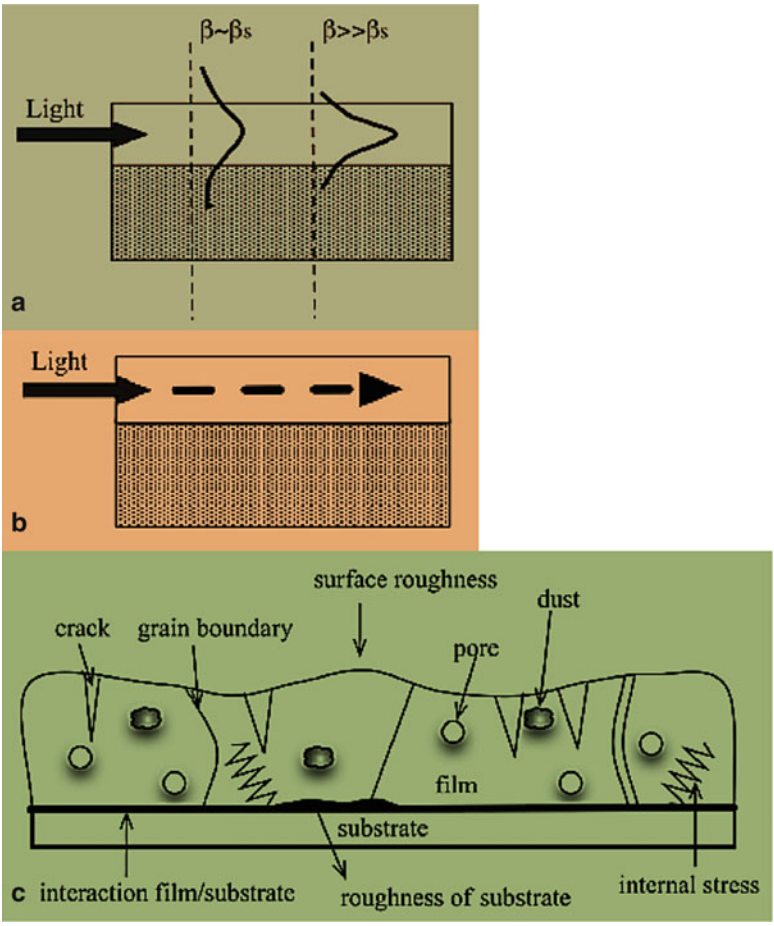

Fig. 2.10 Schematic illustration of propagation losses (Wu 2005): (**a**) the electromagnetic field distribution of waveguide; (**b**) propagation loss by absorption; and (**c**) the different structural and textural defects resulting in propagation losses by diffusion

is commonly observed in semiconductor waveguides. In addition, the impurities contained in waveguide may also induce propagation losses by absorption such as organic residues and doped ions. For example, the Tb^{4+} ions absorb in the range between 400 and 600 nm which increases largely this type of loss when the working wavelength drops into this range. The propagation losses by mode conversion result from the transformation between the excited mode and another guided mode, which involves a propagation loss by a transfer of energy. This effect is predominately caused by the existence of film imperfections such as the inhomogeneity of refractive index or a large surface roughness. This mode conversion does not create a substantial loss when a waveguide is simply used for light power transmission. However, it is still an important factor in a device where a guided mode performs a function, such as curved waveguides (Wu 2005).

2.4.3 Propagation Losses by Diffusion

The light diffusion involves mainly the imperfections at the interfaces (waveguide/substrate and waveguide/cladding layer) or inside the waveguides. These imperfections limit the light propagation because they partially diffuse of light by radiation mode. The potential imperfections appear in the waveguides in the form of porosity, cracks, grain boundaries for polycrystalline films, dust contamination, and so on. Such imperfections could be possibly produced for any deposition operation. For instance, very strict care during the sol–gel coating procedure is helpful to reduce such film imperfections. However, some of the imperfections such as pores and cracks are unavoidable, especially for sol–gel-derived waveguides. The sol–gel elaboration involves organic compounds which must be eliminated by heat treatment. With the removal of organic residues, the sol–gel waveguide is often porous and requires a high temperature of annealing treatment to densify the films, however, the cracks sometimes occur due to the difference of thermal expansion coefficient of the sol–gel layer and substrate which induces the internal stress within the film. Moreover, this light diffusion tends to increase with $1/\lambda$. According to Rayleigh's law, when the imperfection size is smaller than λ, the light diffusion is roughly proportional to $(1/\lambda)^4$. Therefore, this diffusion can be reduced at the longer wavelength range yielding weaker propagation loss. Actually, the inhomogeneities within the waveguide and the irregularity of the interface are the major causes of propagation loss by diffusion. They are mostly related to the elaboration process of waveguides. The principal types of film defects that may induce losses by diffusion are depicted in Fig. 2.10c. They may come from textural defects (cracks, pores, dust, and surface roughness), compositional defects (inhomogeneous nucleation, discontinuous index, or thickness), or structural defects (grain boundaries, internal stress, interaction between film and substrate, etc.). The size and the optical properties of these imperfections dominate their degree of participation for the diffusion loss with the working wavelength. Practically, it has been proved that the mean crystallite size of sol–gel waveguides has to be as low as possible. A nanocrystal larger than 10–15 nm drastically increases the propagation losses. It should be noted that the propagation losses always exist in different degrees whatever the elaboration methods. Through an understanding of the structural and textural imperfections which could produce the propagation losses it is possible to optimize the elaboration process to avoid or at least reduce such factors and obtain a good quality waveguide. This is an important and difficult challenge which must be solved for practical waveguide applications (Wu 2005).

2.4.4 Measurement of Propagation Losses

As the optical attenuation in the waveguide is an important parameter describing the performance of optical integrated devices, a fast and reliable loss measurement technique is a great asset when investigating loss mechanism. A few methods of loss measurement have been carried out.

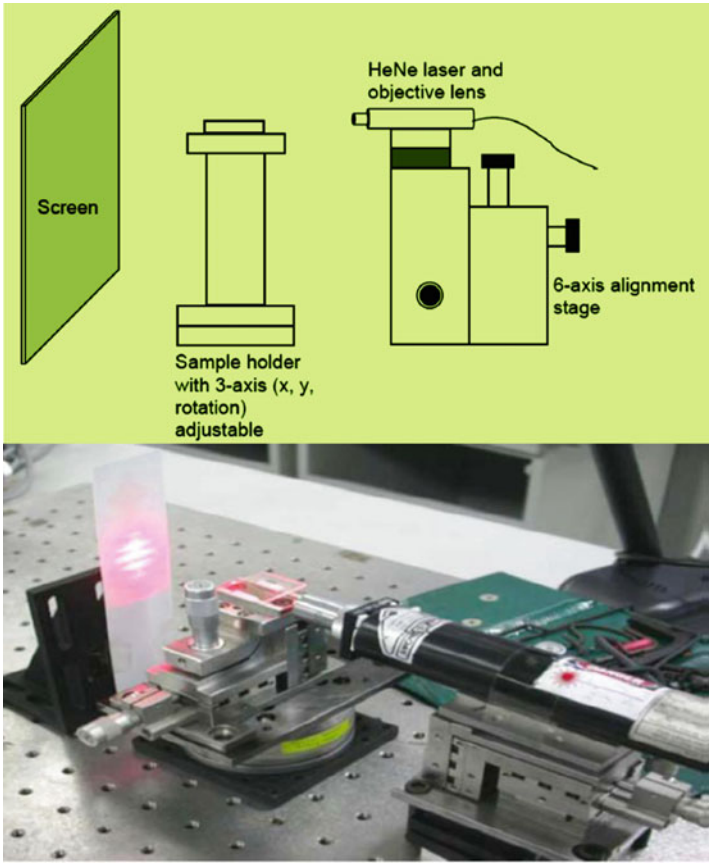

Fig. 2.11 Illustration of cutback method (Wu 2005)

2.4.4.1 Cutback Method

Cutback method is a simple method for direct measurement of transmission losses by comparing the transmittances of waveguides having different lengths. However, it is rather difficult to prepare many waveguides having equal quality and different lengths. Thus, the measurement is done by cutting a waveguide to change the length. A series of transmitted power measurements is performed starting with a relatively long waveguide sample, then after shortening the sample by cleaving and polishing the facet of the waveguide edges. For reasonable accuracy, the measurement must be carried out at each sample length under conditions of optimum coupling efficiency between the incident power and the power propagating in the waveguide. The input power must be constant. A guided wave is excited by end-fire coupling and butt-coupling. A light wave with profile similar to the guided mode profile is fed onto a waveguide end face normal to guided wave propagation. Coupling is localized at the waveguide end. For example, end-fire coupling has been carried out for the wavelength 633 nm. As shown in Fig. 2.11, the channel

waveguide sample was fixed on a sample holder using double-sided tape. The stage could be adjusted on three axes, x, y, and rotation for the alignment purpose. The light source is a helium–neon (He–Ne) laser which emitting light at wavelength around 633 nm with light output 4 mW. The light emitted from the laser was focused using a $\times 10$ objective lens with 16.5 mm focal length mounted on the laser tube. The laser was set on a six axes micro-positioning alignment stage to facilitate the critical alignment required. By adjusting the laser tube from the sample to a distance which is the focal length of the lens, the laser beam was focused on the input facet of the sample. The output emission was projected on white screen. From the pattern of the emission, the coupling of light can be inspected and optimized. The output power can be measured by an optical power meter after the light was coupled into the waveguide. Since the light at wavelength 1,550 nm is invisible, it is difficult to be observed in the end-fire coupling method to optimize the coupling. The loss measurement at wavelength 1,550 nm can be done using butt-coupling, which basically consists on direct heading of the fiber optics to the waveguide. After cutting the waveguide to shorten the length, the transmittance was measured again. Transmission losses are given by (Wu 2005)

$$\alpha = \left| \frac{10 \log\left(\frac{P_1}{P_2}\right)}{\left(\frac{L_1}{L_2}\right)} \right| \quad (\mathrm{dB/cm}) \tag{2.23}$$

where L_1, L_2 (cm) and P_1, P_2 are the lengths and transmittances for before and after cutting, respectively. High quality waveguide edges must be prepared so that the equal input–output coupling efficiencies may be reproduced for each measurement. The drawback of this technique is a destructive method, application is limited to cases where a high quality waveguide edge can be prepared by cleaving, and information about the mode-order dependence losses cannot be obtained.

2.4.4.2 Sliding-Prism Method

The drawback of cutback method can be eliminated by using prism coupler. The attenuation of slab waveguide can be measured using the sliding-prism method. The measurement set up is shown in Fig. 2.12 (Wu 2005). The slab waveguide was clamped firmly below a prism. By tightening the screw, the gap between the waveguide and the prism could be minimized. In order to achieve prism coupling to either the substrate modes or the guided modes, the prism to the waveguide contact must be extremely good since the evanescent field penetration depth is only about 1 μm. The prism surface must be dirt free. In addition, optimum coupling is only achieved at the point of closest contact, where the screw clamp applies the greatest pressure to the sample, and at a point as near to the right angled edge of the prism as possible to limit the degree of return coupling to the prism. The prism coupling assembly was then set on a rotational stage which was mounted on an x–y

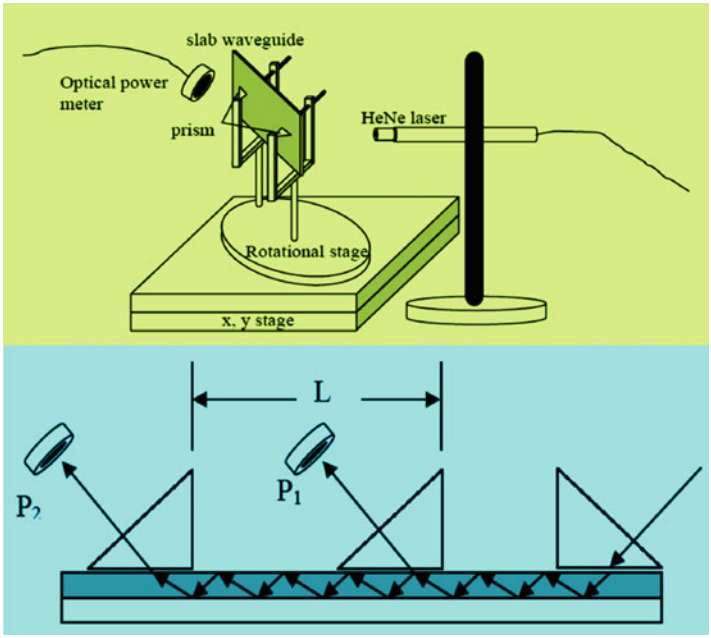

Fig. 2.12 Schematic illustration of sliding-prism method (Wu 2005)

translational stage. A He–Ne laser with an objective lens mounted on it was set at the same level with the prism. The rotational stage was adjusted to couple the light into the waveguide at certain incidence angle of the laser beam. The light was coupled into the waveguide once a bright laser line (guided mode) appeared in the waveguide. The rotational stage was locked to keep the coupling of light at that incidence angle. In order to couple out the light, a second prism was then clamped to the waveguide to interact with the guided mode at a distance of about 1–2 cm from the input prism. The light was coupled out once the optical contact was sufficiently good and the mode lines (m lines) observed on a screen. The output power was then measured using an optical power meter. The second prism was slide backward for a desired distance and the output power was measured and the detected power the two locations were compared. An important requirement is that nearly 100 % output efficiency must be maintained during the measurement in order to maintain constant coupling efficiency (Wu 2005).

2.4.4.3 Fabry–Perot Resonances

A waveguide can be seen as a Fabry–Perot cavity with two polished facets acting as two mirrors. Therefore, it is possible to measure the propagation loss using these Fabry–Perot resonances. If R is denoted as the facet reflectivity, the ratio of the output and the input powers can be given by (Yin 2009)

$$\frac{P_{\text{out}}}{P_{\text{in}}} = \frac{(1-R)^2 \mathrm{e}^{-\alpha L}}{(1-R\mathrm{e}^{-\alpha L})^2 + 4R\mathrm{e}^{-\alpha L}\sin^2(\phi/2)} \tag{2.23a}$$

where R for TM and TE modes is given by Fresnel's equations. Assuming that light is coupled into the waveguide at normal incidence, then R can be simply expressed as $R = (n-1)^2/(n+1)^2$. $\phi = 2nkL\cos\theta + \phi_{\text{r}}$ is the phase difference associated with optical path difference of the resonator, and $\theta \approx 0$ is the incident angle. Given $\zeta = \dfrac{I_{\max}}{I_{\min}} = \dfrac{(1+R\mathrm{e}^{-\alpha L})^2}{(1-R\mathrm{e}^{-\alpha L})^2}$ as the ratio of the maximum intensity to the minimum intensity, the propagation loss α can be expressed as (Yin 2009)

$$\alpha = -\frac{1}{L}\ln\left(\frac{1}{R}\frac{\sqrt{\zeta}-1}{\sqrt{\zeta}+1}\right) \tag{2.23b}$$

The measurement using Fabry–Perot resonance can be more stable or repeatable and more accurate than using the cutback method.

2.4.4.4 Scattered Light Measurement

The propagation loss of a waveguide can also be known by measuring the scattered light from the surface of the waveguide. The assumption of this method is that the amount of light scattered from the surface is proportional to the light propagating inside the waveguide. Then the rate that the scattered light decays should mimic the decaying rate of the propagated light inside the waveguide. Optical fibers can be used to collect the scattered light and can be scanned along the surface of the waveguide (Yin 2009).

2.5 Optoelectronic Characterization

2.5.1 Optical Power Meters

Optical power meter is the simplest and most basic piece of equipment for optoelectronic characterization, as shown in Fig. 2.13. Different models have different connector types and are specialized to either multi-mode or single-mode fiber or optical waveguide. There is always a wavelength switch to adjust the power readings for the particular wavelength being received. Also there is usually a range switch which determines the range of signal power expected—although this last function can be automatically determined by the meter itself (Dutton 1998).

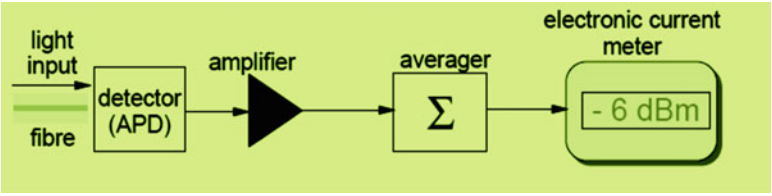

Fig. 2.13 Optical power meter—logical structure (Dutton 1998)

2.5.2 *Optical Time-Domain Reflectometers (OTDRs)*

The OTDR can be used to look at a fiber link from inside the fiber. In reality it is just a radar system for looking at fiber. High intensity pulses are sent into the fiber from a specialized laser and when the pulse returns its strength is displayed on an oscilloscope screen in the form of a trace. A schematic of such a display is shown in Fig. 2.14. In the trace reflections can be seen coming from all along the fiber itself. This is the result of Rayleigh scattering. Every time there is a discontinuity or imperfection in the fiber/waveguide the effect can be seen in the trace. Such events can be the presence of a connector or a splice or some more serious imperfection such as a crimp in the cable due to poor installation. OTDR can be used to quickly determine the length of the fiber, attenuation in decibel of the whole fiber link and the attenuation of separate sections of fiber (if any), attenuation characteristics of the basic fiber itself, locations of connectors, joints and faults in the cable. Many OTDRs come with additional functions such as optical power meter or laser source so that a good OTDR often has all of the function needed in the field. In addition many OTDRs offer computer output so that collect OTDR data can be collected in the form of digital readings and analyze it later on a computer (Dutton 1998).

2.5.3 *Spectrum Analyzers*

A spectrum analyzer scans across a range of wavelengths and provides a display showing the signal power at each wavelength. Figure 2.15 shows a simplified example of the kind of display produced by a typical spectrum analyzer. From this display the following parameters can be calculated: The power levels of each channel, spectral width of each channel, any interference between channels such as crosstalk possibilities, by connecting it in different places through the system many potential problems can be tracked such as laser drift, etc. (Dutton 1998).

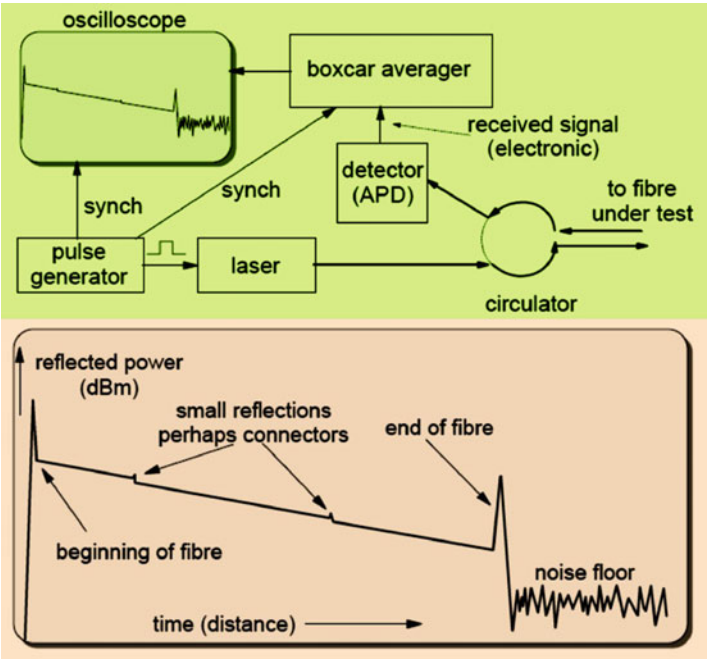

Fig. 2.14 Schematic illustration of optical time-domain reflectometer (Dutton 1998)

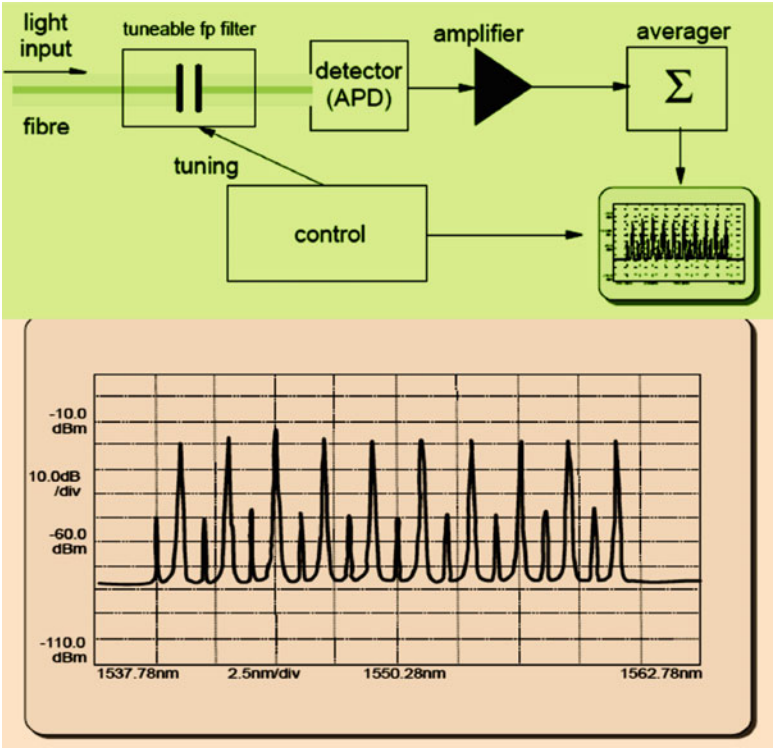

Fig. 2.15 Illustration of spectrum analyzer (Dutton 1998)

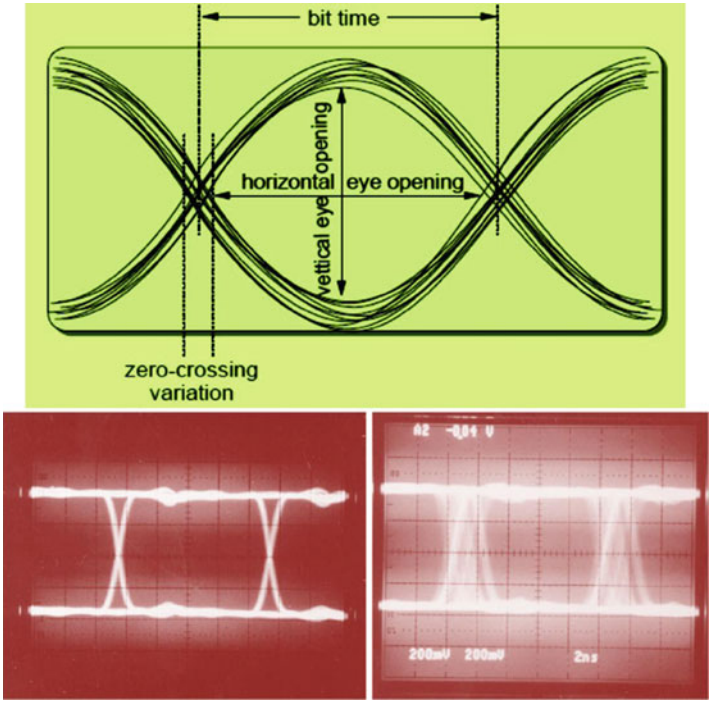

Fig. 2.16 Illustration of eye diagrams (Dutton 1998)

2.5.4 Eye Diagrams

The eye diagram has become the recognized way of looking at an electronic signal and determining its "goodness" as a carrier of information. It consists of many (from hundreds to millions) of instances of the signal displayed over the top of one another. In extremely fast equipment only one or two points might be got on a trace at a single sweep. But displaying them together allows assessing the quality of the received signal very well indeed. As shown in Fig. 2.16 (Dutton 1998), the diagram is produced by feeding the result of the analogue section of the receiver circuit to the *y*-axis control of an oscilloscope. The sweep is set to display one full cycle (two-bit times) and is usually triggered from the receiver's PLL circuit (the receiver's derived clock).

The eye diagram has the following important aspects (Dutton 1998): (a) The vertical eye opening indicates the amount of difference in signal level that is present to indicate the difference between one-bits and zero-bits. The bigger the difference the easier it is to discriminate between one and zero. Of course this is affected significantly by noise in the system. (b) The horizontal eye opening indicates the

amount of jitter present in the signal. The wider the eye opening is on this axis the less problem likely has with jitter. (c) The thickness of the band of signals at the zero-crossing point is also a good measure of jitter in the signal. (d) The best indication of signal "goodness" is just the size of the eye opening itself. The larger it is the easier it will be to detect the signal and the lower will be the error rate. When the eye is nearly closed it will be very difficult or impossible to derive meaningful data from the signal.

2.6 Electro-optic Effects

An electro-optic effect is a change in the optical properties of a material in response to an electric field that varies slowly compared with the frequency of light. The term encompasses a number of distinct phenomena, which can be subdivided into: (a) Change of the absorption: (i) Electroabsorption—general change of the absorption constants. (ii) Franz–Keldysh effect—change in the absorption shown in some bulk semiconductors. (iii) Quantum-confined Stark effect—change in the absorption in some semiconductor quantum wells. (iv) Electrochromic effect—creation of an absorption band at some wavelengths, which gives rise to a change in color. (b) Change of the refractive index: (i) Pockels effect (or linear electro-optic effect)—change in the refractive index linearly proportional to the electric field. Only certain crystalline solids show the Pockels effect, as it requires lack of inversion symmetry. (ii) Kerr effect (or quadratic electro-optic effect, QEO effect)—change in the refractive index proportional to the square of the electric field. All materials display the Kerr effect, with varying magnitudes, but it is generally much weaker than the Pockels effect. (iii) Electro-gyration—change in the optical activity. Changes in absorption can have a strong effect on refractive index for wavelengths near the absorption edge, due to the Kramers–Kronig relation.

Using a less strict definition of the electro-optic effect allowing also electric fields oscillating at optical frequencies, one could also include nonlinear absorption (absorption depends on the light intensity) to category (a) and the optical Kerr effect (refractive index depends on the light intensity) to category (b). Combined with the photoeffect and photoconductivity, the electro-optic effect gives rise to the photorefractive effect.

An electric field E applied to a transparent material generally modifies the refractive index n_0 for a particular mode of propagation in accordance with the equation (Kaye & Laby 2012)

$$\frac{1}{n^2} = \frac{1}{n_0^2} + rE + RE^2 + \cdots \tag{2.24}$$

In amorphous materials or centro-symmetric crystals the coefficients of odd powers of E are zero, and the first nonzero term RE^2 represents the quadratic Kerr effect, usually characterized for a particular material by the Kerr constant:

$$B = \frac{\Delta n}{\lambda_0 E^2} = \frac{n_0^3}{2\lambda_0} R \tag{2.25}$$

where λ_0 is the free-space wavelength.

For the case of a birefringent crystal, the field E modifies the index ellipsoid $\sum_{i=l}^{3}(x_i^2/n_i^2) = 1$, in the principal axis coordinate system, to (Kaye & Laby 2012):

$$\sum_{i=1}^{3}\sum_{j=1}^{3}\sum_{k=1}^{3}\sum_{l=1}^{3}\left(\frac{1}{n_{ij}^2} + r_{ijk}E_k + R_{ijkl}E_kE_l + \cdots\right)x_ix_j = 1 \tag{2.26}$$

where $n_{ij} = n_i$, for $i = j$, and $1/n_{ij} = 0$ for $i \neq j$. From a knowledge of the change in orientation and dimensions of the index ellipsoid, as given by this equation, the field-induced birefringence for a ray of given direction and polarization may be calculated.

In practice the electrooptic effect is either predominantly linear or quadratic in E, and is therefore characterized by either r_{ijk} or R_{ijkl}, depending on the material. Since r_{ijk} is symmetrical in i, j, and R_{ijkl}, symmetrical in i, j and in k, l, pairs of values i, j and k, l are denoted by indices m and n respectively, which run from 1 to 6 according to the scheme (Kaye & Laby 2012):

$$1 \leftrightarrow 1,1 \quad 2 \leftrightarrow 2,2 \quad 3 \leftrightarrow 3,3 \quad 4 \leftrightarrow 2,3 \quad 5 \leftrightarrow 1,3 \quad 6 \leftrightarrow 1,2$$

When measured at low frequencies ($<10^4$ Hz), the coefficients may include contributions from the elasto-optic effects of piezoelectric and/or electrostrictive strains. The linear electro-optic effect observed at frequencies sufficiently high for these contributions to be negligible is called the Pockels effect. The strain effects may contribute up to 50 % of the low-frequency effect.

The quadratic effect is exhibited most markedly by materials in which the permittivity is high and varies rapidly with temperature. Here, since the R_{mn} vary accordingly, it is more convenient to replace $R_{mn}\,E_kE_l$ in the equation of the index ellipsoid by $g_{mn}P_kP_l$ (where $P = D - \varepsilon_0 E$), and to express the properties of the material in terms of g_{mn}. Typical parameters for selected electrooptic materials at low frequencies are given in Table 2.2 (Kaye & Laby 2012).

The indicatrix and electrooptic coefficients are referred to the usual crystallographic coordinate system. $Ox_3 \equiv Oz$ is the fourfold axis for cubic and tetragonal symmetries, or the threefold axis for trigonal symmetry; $Ox_1 \equiv Ox$; $Ox_2 \equiv Oy$, except for the trigonal case in which Ox_1 is perpendicular to the mirror plane. For uniaxial crystals $n_1 = n_1 = n_0$, $n_3 = n_e$. The half-wave voltage V_π is used conventionally to characterize the sensitivity of an electrooptic material. It is the voltage required to obtain one half-wavelength of optical path difference between the two

Table 2.2 Properties of selected electrooptic materials at a wavelength of 633 nm (Kaye & Laby 2012)

Material	Point-group symmetry	Electrooptic coeff. and value: low freq. $\frac{r}{10^{-12}\ \mathrm{m/V^{-1}}}$ or $\frac{g}{\mathrm{m^4/C^{-2}}}$	High freq. value	Refractive index	Relative permittivity (LF)	Relative permittivity (HF)
$C_6H_5O_2N$ (nitrobenzene)	∞	$B = 4.4 \times 10^{-12}\ \mathrm{m/V^{-2}}$		1.55	35.7	
$pb_{0.814}La_{0.124}$–$(Ti_{0.6}Zr_{0.4})O_3$ (PLZT)	∞	$n_e^3 r_{33} - n_0^3 r_{33} = 2320$ [1]		$n_0 = 2.55$		
β-Zns	$\bar{4}3m$	$r_{41} = 2.1$	−1.6	2.35	16	12.5
ZnSe	$\bar{4}3m$	$r_{41} = 2.0$	2.0	2.60	9.1	9.1
ZnTe	$\bar{4}3m$	$r_{41} = 4.04$	4.3	2.99	10.1	10.1
$Bi_{12}SiO_{20}$	23	$r_{41} = 5.0$		2.54		
KH_2PO_4 (KDP)	$\bar{4}2m$	$r_{41} = 8$		$n_0 = 1.5074$	$\varepsilon_1, \varepsilon_2 = 42$	44
		$r_{63} = 11$		$n_e = 1.4669$	$\varepsilon_3 = 21$	21
KD_2PO_4 (KD*P)	$\bar{4}2m$	$r_{41} = 8.8$ [1]		$n_0 = 1.502$	$\varepsilon_1, \varepsilon_2 = 58$	
		$r_{63} = 24.1$		$n_e = 1.462$	$\varepsilon_3 = 50$	48
CsH_2AsO_4 (CDA)	$\bar{4}2m$	$r_{41} = 14.8$ [2]		$n_0 = 1.572$		
		$r_{63} = 18.2$ [2]		$n_e = 1.550$		
$BaTiO_3$	$m3m$	$g_{11} - g_{12} = 0.13$		2.437		4,500
$SrTiO_3$	$m3m$	$g_{11} - g_{12} = 0.14$		2.38		300
$KTa_{0.35}Nb_{0.65}O_3$ (KTN)	$m3m$	$g_{11} = 0.136$		2.29	$\approx 10^4$	
		$g_{12} = -0.038$				
		$g_{44} = 0.147$				
$Ba_{0.25}Sr_{0.75}Nb_2O_6$	$4mm$	$r_{13} = 67$		$n_0 = 2.312$	$\approx 2 \times 10^4$	3,400
		$r_{33} = 1{,}340$		$n_e = 2.299$		
		$r_{51} = 42$				
		r_c	1,090			

(continued)

Table 2.2 (continued)

Material	Point-group symmetry	Electrooptic coeff. and value: low freq. $\frac{r}{10^{-12}\,\mathrm{m/V^{-1}}}$ or $\frac{g}{\mathrm{m^4/C^{-2}}}$	High freq. value	Refractive index	Relative permittivity (LF)	Relative permittivity (HF)
$LiNbO_3$	$3m$	$r_{13} = 9.6$	8.6	$n_0 = 2.286$	$\varepsilon_1, \varepsilon_2 = 78$	
		$r_{22} = 6.8$	3.4	$n_e = 2.200$		43
		$r_{33} = 30.9$	30.8		$\varepsilon_3 = 32$	28
		$r_{51} = 32.6$	28			
		$r_c = 21.1$				
$LiTaO_3$	$3m$	$r_{13} = 8.4$	7.5	$n_0 = 2.176$	$\varepsilon_1, \varepsilon_2 = 51$	
		$r_{22} = -0.2$	1	$n_e = 2.180$		41
		$r_{33} = 30.5$	33		$\varepsilon_3 = 45$	43
		$r_c = 22$	–			
		r_{51}	20			
Ag_3AsS_3	$3m$	r_{22}	1.1	$n_0 = 3.018$		
		r_c	3.4	$n_e = 2.739$		
$KNbO_3$	$2mm$	$r_{13} = 28$		$n_1 = 2.280$		
		$r_{23} = 1.3$		$n_2 = 2.329$		
		$r_{33} = 64$		$n_3 = 2.169$		
		$r_{42} = 380$				
		$r_{51} = 105$	270			

Table 2.3 Birefringence for commonly used configurations (Kaye & Laby 2012)

Material symmetry	Light direction	Field direction	Induced birefringence Δn
∞	Any	Transverse	$B\lambda_0 E^2$
$\bar{4}2$	Oz	Oz	$n_0^3 r_{63} E_3$
$\bar{4}3m$	Ox	Oz	$n_0^3 r_{41} E_3$
$m3m$	Ox	Oz	$n_0^3 (g_{11} - g_{12}) P_3^2/2$
$3m$	Ox	Oz	$n_3^3 \left\{ r_{33} - \left(\frac{n_1}{n_3}\right) r_{13} \right\} E_3/2 = \frac{1}{2} n_3^3 r_{33} E_3$
$4mm$	45° to Oz	45° to Oz longitudinal	$\left(n_3^3/4\sqrt{2}\right)(r_{13} - r_{33})E$

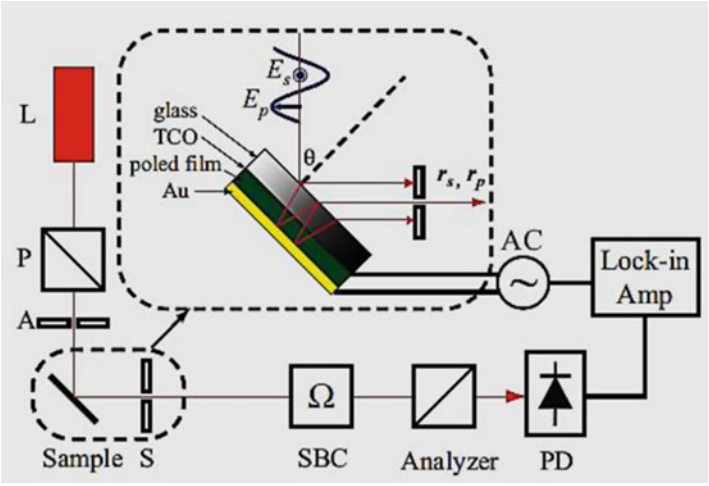

Fig. 2.17 Schematic illumination of the Teng–Man measurement setup: *L* laser, *P* polarizer, *A* aperture, *S* slit, *SBC* Soleil-Babinet Compensator, *PD* photodetector (Park 2008)

vibration components of a wavefront, using a cube of the material of side 1 cm with specified directions of light and applied field. Table 2.3 gives the induced birefringence for a number of commonly used configurations (Kaye & Laby 2012).

The electro-optic effect can be determined by measuring the change of the dielectric constant or index of refraction when a field is applied across the nonlinear electrooptical material of interest. There are various techniques for characterization of electro-optic effect, including Mach–Zehnder (MZ) interferometry, Fabry–Perot (FP) interferometry, attenuated total reflection (ATR), waveguide method, and two slit interference method. One of the most popular measurement techniques is called Teng–Man reflection method. Figure 2.17 shows the schematic illumination of the Teng–Man measurement setup (Park 2008). 45° polarized light is incident at an angle on the multilayered sample structure containing nonlinear electrooptical thin film. For the polymer material, it is usually spin-coated on a glass substrate

with transparent conducting oxide (TCO), commonly indium tin oxide (ITO), and poled electrically to generate the second-order nonlinearity. The first reflection off the air–glass interface and subsequent beams resulting from reflection of the first pass on its way out at the glass/air interface back into the polymer film and out again are blocked. The remaining light reflected off the sample experiences an additional controllable phase retardation introduced by a Soleil-Babinet Compensator (SBC). The intensity of the light is detected after passing through the analyzer using a lock-in amplifier. At each angle of incidence, two different data sets, the optical bias curve I_{dc} (Ω) and the modulated intensity I_m (V, Ω) are collected. The optical bias curve is the intensity profile obtained by varying the retardation generated by the SBC with no applied voltage to the sample, while the modulation data sheet is obtained by applying an AC voltage $V\sin(\omega t)$ to the sample and using a lock-in amplifier synced to the fundamental frequency of the applied voltage to record the resulting modulation of I_{dc} (Ω) for a given retardation. I_{dc} (Ω) can be expressed in terms of the complex reflection coefficients r_s and r_p of the s- and p-polarized waves, the intensity of the incident laser I_0, and the phase retardation Ω. The electric field at the photodetector can be expressed by (Park 2008)

$$\begin{pmatrix} E_x \\ E_y \end{pmatrix} = \frac{E_0}{2}\begin{pmatrix} 1 & 1 \\ 1 & 1 \end{pmatrix}\begin{pmatrix} e^{i\Omega} & 0 \\ 0 & 1 \end{pmatrix}\begin{pmatrix} r_s & 0 \\ 0 & -r_p \end{pmatrix}\begin{pmatrix} \frac{1}{\sqrt{2}} \\ \frac{1}{\sqrt{2}} \end{pmatrix} \tag{2.27}$$

where the first 2×2 matrix represents the crossed polarizer, the second one the SBC, the third the reflectance from the sample, and the last 2×1 matrix the vector for 45° polarized light after the 45° polarizer. The first 2×2 matrix representation for the crossed polarizer doesn't look crossed compared to the input polarization. This is because the y-axis (horizontal) of the coordinate system is flipped after the reflection. For the same reason, the sign of the r_p is the minus in the third matrix for the reflectance from the sample. The measured optical intensity, I, is proportional to the square of the electric field, $\left|\overline{E}\right|^2 = E_x^2 + E_y^2$. Varying the optical bias Ω generates the optical bias curve, which is given by (Park 2008)

$$I_{dc} = \frac{I_0}{4}\left|r_s e^{i\Omega} - r_p\right|^2 = A + B\sin^2\left(\frac{\Psi_{sp} + \Omega}{2}\right) \tag{2.28}$$

where $A = \frac{I_0}{4}\left(|r_s|^2 - |r_s|^2\right), B = I_0|r_s|\left|r_p\right|$, $r_s = |r_s|e^{i\Psi_s}$, $r_p = \left|r_p\right|e^{i\Psi_p}$, and $\Psi_{sp} = \Psi_s - \Psi_p$.

To first order in V, the modulated intensity $I_m(V, \Omega)$ is obtained by differentiating (2.28) to get (Park 2008)

$$I_{\mathrm{m}} = \delta A + \delta B \sin^2\left(\frac{\Psi_{\mathrm{sp}} + \Omega}{2}\right) + \frac{B}{2}\sin\left(\Psi_{\mathrm{sp}} + \Omega\right)\delta\Psi_{\mathrm{sp}} \tag{2.29}$$

where $\delta\Psi_{\mathrm{sp}} = \frac{I_{\mathrm{m}}\left(\frac{\pi}{2}\right) - I_{\mathrm{m}}\left(\frac{3\pi}{2}\right)}{2I_{\mathrm{c}}}$, and $\frac{\delta B}{B} = \frac{I_{\mathrm{m}}(\pi) - I_{\mathrm{m}}(0)}{2I_{\mathrm{c}}}$. Typically, in the Teng–Man method, I_{m} is measured only at points 1 and 2 as a function of voltage and the average of the difference in the slopes in the plot of I_{m} versus V to extract $\delta\Psi_{\mathrm{sp}}$. Usually, I_{m} is positive at point 1 and negative ant point 2 or vice versa. But this is not always the case so care must be taken to note the phase of the reading on the lock-in amplifier, synced to the fundamental frequency of the applied voltage $V\sin(\omega t)$. A similar technique can be applied to obtain $\delta B/B$ from data at points 3 and 4 (Park 2008).

2.7 Thermo-optic Effects

Thermo-optic effect in the materials indicates the change of refractive index as a function of temperature change ($\mathrm{d}n/\mathrm{d}T$). It can be used in fabrication of digital optical switch, Mach–Zehnder interferometer type optical switch and optical cross-connect and waveguides. Those optical devices play a key function in communication network because of their control over the optical path by changing the temperature. Although many electro-optic devices have been well known for their fast reaction rate, their polarization change has always been a problem. That is the reason why thermo-optic devices have become of great interest in the application areas because of their advantage of polarization insensitive characteristics. The factors that decide thermo-optic effect ($\mathrm{d}n/\mathrm{d}T$) are density and electronic polarizability change with temperature (Kang et al. 2002):

$$\frac{\mathrm{d}n}{\mathrm{d}T} = \frac{(n^2-1)(n^2+2)}{6n}(\varphi - \alpha) \tag{2.30}$$

where φ is the temperature coefficient of the electronic polarizability, and α is the thermal expansion coefficient. When the electronic polarizability term is dominant, the refractive index becomes positive and increases with temperature. On the other hand, $\mathrm{d}n/\mathrm{d}T$ becomes negative and decreases with increasing temperature when thermal expansion term is dominant. In general, $\mathrm{d}n/\mathrm{d}T$ of inorganic glasses is decided by the competition between φ and α. However, in the case of optical polymers, $\mathrm{d}n/\mathrm{d}T$ exclusively depends on thermal expansion term because their α is always much higher than their φ. This is the reason why most optical polymers have a negative $\mathrm{d}n/\mathrm{d}T$.

Optical waveguides for fabrication of thermo-optic switches have used the materials of silica and optical polymers. The main advantages of silica-based thermo-optic switch are their easier fiber connection, lower optical loss, and better thermal stability. However, it typically requires high switching power of about 0.4–0.5 W and exhibits long response time in the order of *ms* because silica has a low $\mathrm{d}n/\mathrm{d}T$ of about $10^{-5}/^{\circ}\mathrm{C}$. The polymer-based thermo-optic switch overcomes the

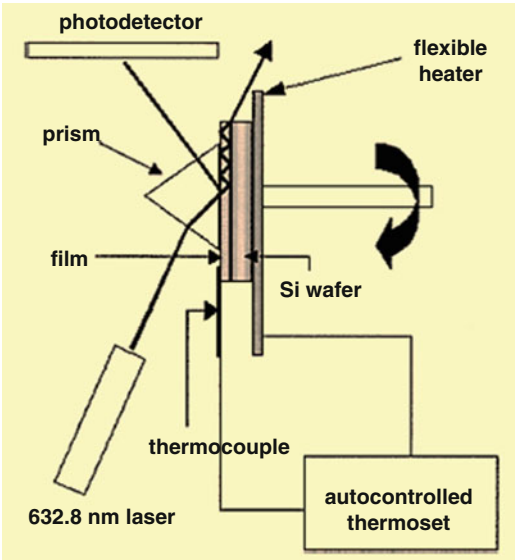

Fig. 2.18 Apparatus for measuring thermo-optic coefficients of the film (Kang et al. 2002)

high switching power of silica-based one due to its higher dn/dT of about -10^{-4}/°C, but then, its thermal stability is another major drawback of practical application. Therefore, sol–gel-derived inorganic–organic hybrid materials composed of silica and organic or polymer has been developed for application of thermo-optic switch in integrated optics. The dn/dT of sol–gel films which are composed of silica and methacrylate group are negative and the order of 10^{-4}/°C. Their high values of dn/dT make them possible in thermo-optic applications. Figure 2.18 shows a schematic diagram of the prism coupler equipped with auto-controlled hot stage to measure the refractive index of films as a function of temperature (Kang et al. 2002). The flexible heater, which is thin enough not to affect the optical coupling between the prism and the film, is used to elevate sample temperature. The film-type thermocouple is attached to sample surface and temperature variation in the prism is neglected over the range of measurement (30–100 °C). Refractive index variation due to film thickness change with temperature can be neglected because it is possible to calculate thickness and refractive index independently using a prism coupler. A He–Ne laser of 632.8 nm wavelength is used as the light source. This method using the prism coupler equipped with an auto-controlled hot stage can provide reliable measurements of dn/dT of the optical waveguide films.

2.8 Acousto-optic Effects

Acousto-optic effects are based on the change of the refractive index of optical waveguide due to the presence of sound waves in that waveguide. These variations in the refractive index, due to the pressure fluctuations, may be detected optically by

refraction, diffraction, and interference effects, reflection may also be used. The acousto-optic effect is extensively used in the measurement and study of ultrasonic waves. However, the growing principal area of interest is in acousto-optical devices for the deflection, modulation, signal processing, and frequency shifting of light beams. This is due to the increasing availability and performance of lasers, which have made the acousto-optic effect easier to observe and measure. Technical progresses in both crystal growth and high frequency piezoelectric transducers have brought valuable benefits to acousto-optic components' improvements. It can be used in nondestructive testing, structural health monitoring, and biomedical applications, where optically generated and optical measurements of ultrasound give a noncontact method of imaging.

The acousto-optic interaction is a more general effect of photoelasticity consisting in the change of the material's permittivity ε under the action of a mechanical strain α. Phenomenologically, this effect is described as variations of the optical indicatrix coefficients B_i caused by the strain α_j (MSU 2013):

$$\Delta B_i = p_{ij}\alpha_j \tag{2.31}$$

where p_{ij} is the photoelastic tensor components $i, j = 1, 2, \ldots, 6$.

In case of the acousto-optic effect, the strains α_j are produced by an acoustic wave excited in a transparent waveguide. Thus, the acoustic wave is accompanied by a wave of refractive index variations. For a plane acoustic wave propagating along the axis z, the refractive index variation can be expressed as (MSU 2013)

$$n(z,t) = n + \Delta n \cos\left(2\pi ft - K_z\right) \tag{2.32}$$

where n is the undisturbed refractive index of refraction, f and K_z are the frequency and propagation constant of the acoustic wave, Δn is the amplitude variation in the refractive index generated by the acoustic wave, and is given as

$$\Delta n = -\frac{1}{2}n^3 pa \tag{2.33}$$

The generated refractive index, $n(z, t)$, gives a diffraction grating moving with the velocity given by the speed of the sound wave in the waveguide. Light which then passes through the transparent waveguide material, is diffracted due to this generated refraction index, forming a prominent diffraction pattern. This diffraction pattern corresponds with a conventional diffraction grating at angles θ_m from the original direction, and is given by (Scruby and Drain 1990)

$$\Lambda = \sin\left(\theta_m\right) = m\lambda \tag{2.34}$$

where λ is the wavelength of the optical wave, Λ is the wave length of the acoustic wave and m is the integer order maximum.

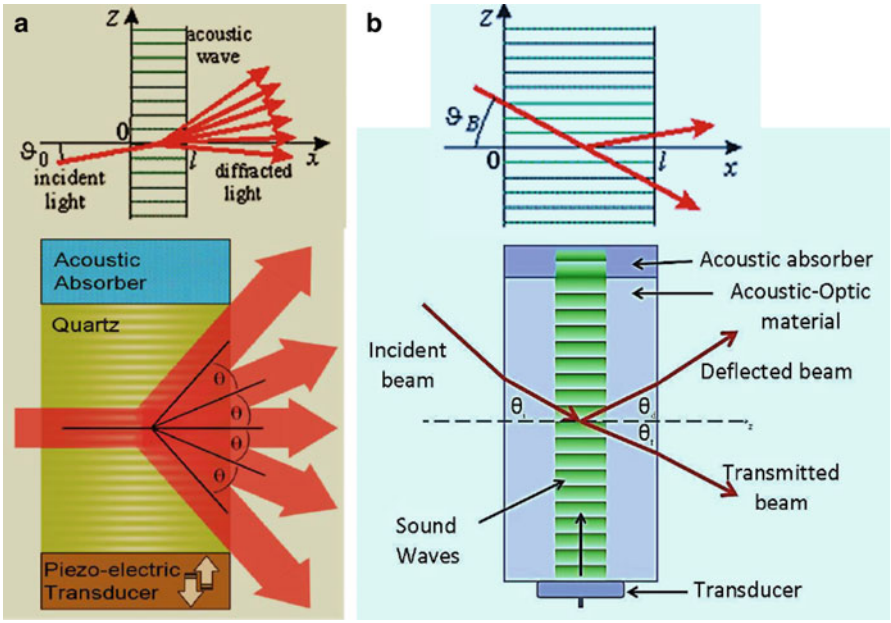

Fig. 2.19 Illustration of acousto-optic effects: (**a**) Raman–Nath diffraction; and (**b**) Bragg diffraction

Light diffracted by an acoustic wave of a single frequency produces two distinct diffraction types. These are Raman–Nath diffraction and Bragg diffraction (Fig. 2.19a, b). Raman–Nath diffraction is observed with relatively low acoustic frequencies, typically less than 10 MHz, and with a small acousto-optic interaction length, ℓ, which is typically less than 1 cm. This type of diffraction occurs at an arbitrary angle of incidence, θ_0. In contrast, Bragg diffraction occurs at higher acoustic frequencies, usually exceeding 100 MHz. The observed diffraction pattern generally consists of two diffraction maxima; these are the zeroth and the first orders. However, even these two maxima only appear at definite incidence angles close to the Bragg angle, θ_B. The first order maximum or the Bragg maximum is formed due to a selective reflection of the light from the wave fronts of ultrasonic wave. The Bragg angle is given by the expression (MSU 2013)

$$\sin\theta_B = -\frac{\lambda f}{2n_i\nu}\left[1+\frac{\nu^2}{\lambda^2 f^2}\left(n_i^2-n_d^2\right)\right] \tag{2.35}$$

where λ is the wavelength of the incident light wave (in a vacuum), f is the acoustic frequency, ν is the velocity of the acoustic wave, n_i is the refractive index for the incident optical wave, and n_d is the refractive index for the diffracted optical waves.

In general, there is no point at which Bragg diffraction takes over from Raman–Nath diffraction. It is simply a fact that as the acoustic frequency increases,

the number of observed maxima is gradually reduced due to the angular selectivity of the acousto-optic interaction. Traditionally, the type of diffraction, Bragg or Raman–Nath, is determined by the conditions $Q \gg 1$ and $Q \ll 1$ respectively, where Q is given by (MSU 2013)

$$Q = \frac{2\pi\lambda l f^2}{n v^2} \tag{2.36}$$

which is known as the Klein–Cook parameter. Since, in general, only the first order diffraction maximum is used in acousto-optic devices, Bragg diffraction is preferable due to the lower optical losses. However, the acousto-optic requirements for Bragg diffraction limit the frequency range of acousto-optic interaction. As a consequence, the speed of operation of acousto-optic devices is also limited.

If the acousto-optic material is optically isotropic, then (2.35) is simplified to (MSU 2013)

$$\sin\theta_B = -\frac{\lambda f}{2nv} \tag{2.37}$$

The utilization of laser has led the development of acousto-optics and its applications, mainly for deflection, modulation, and signal processing. Technical progresses in both crystal growth and high frequency piezoelectric transducers have brought valuable benefits to improvements of acousto-optic components. Some materials displaying acousto-optic effect include fused silica, lithium niobate, arsenic trisulfide, tellurium dioxide and tellurite glasses, lead silicate, $Ge_{55}As_{12}S_{33}$, mercury(I) chloride, lead(II) bromide, and other materials. Although acoustic interactions can be observed in liquids, practical devices use crystals or glasses as the interaction medium, with RF frequencies in the MHz to GHz range. Table 2.4 shows standard characteristics of the main materials used in acousto-optics (AA Sa 2013).

2.9 Nonlinear Optic Effects

Nonlinear effects can have a significant impact on light propagation in waveguides. While the nonlinear response of waveguides like optical fibers is relatively weak, tight confinement of light in a micron-size core together with long propagation distances (100 km and more) result in significant nonlinear interactions. Nonlinear effects can be both advantageous and detrimental for waveguide devices and transmission systems. On the one hand, nonlinear effects enable new functionalities and devices, such as switching, supercontinuum generation, wavelength conversion, fiber lasers, amplifiers, logic devices, and soliton transmission systems. At the same time, they may be detrimental for optical communication systems.

Table 2.4 Standard characteristics of the main materials used in acousto-optics (AA Sa 2013)

Material	Type	Optimum optical range for acousto-optic applications (nm)	Incident optical polarization[a]	Refractive index	Max CW laser power density (W/mm^2)	Acoustic velocity (m/s)
Ge	Crystal	2,500–11,000	Linear $\parallel$	4 @ $\lambda = 10{,}600$ nm	5	5,500
Doped glass	Glass	500–650	Unpolarized	2.09 @ $\lambda = 633$ nm	1	3,400
$Ge_{33}As_{12}Se_{55}$	Glass	1,100–1,700	Unpolarized	2.59 @ $\lambda = 1{,}064$ nm	1	2,520
As_2S_3	Glass	700–900	Unpolarized	2.46 @ $\lambda = 1{,}150$ nm	1	2,600
$PbMoO_4$	Crystal	480–1,100	Unpolarized	2.26/2.38 @ $\lambda = 633$ nm	0.5	3,630
TeO_2	Crystal	450–1,100	Linear $\perp$	2.26 @ $\lambda = 633$ nm	5	4,200
TeO_2	Crystal	350–4,500	Linear-circular	2.26 @ $\lambda = 633$ nm	5	620
SiO_2 (fused silica)	Glass	200–2,200	Linear $\perp$	1.46 @ $\lambda = 633$ nm	>100	5,960
SiO_2 (fused silica)	Glass	200–2,200	Unpolarized	1.46 @ $\lambda = 633$ nm	<100	3,760

[a] $\parallel$ and $\perp$ means parallel and perpendicular to the acoustic wave direction for optimum acousto-optic coupling

At high intensities, light–matter interactions become nonlinear as a result of harmonic motion of bound electrons in the applied field. As a result, the induced polarization can be written as (Litchinitser and Iakhnine 2011)

$$P(t) = \chi^{(1)}E(t) + \chi^{(2)}E^2(t) + \chi^{(3)}E^3(t) + \cdots \tag{2.38}$$

where $\chi^{(1)}$ is the linear susceptibility, and $\chi^{(2)}$ and $\chi^{(3)}$ are the second- and third-order nonlinear optical susceptibilities. For simplicity, in (2.38) it is assumed that both P and E are scalar, and the medium is dispersionless and lossless. In the most general case, $\chi^{(i)}$ are tensors of rank $j + 1$ and are frequency dependent. The second-order susceptibility, which is responsible for such effects as second-harmonic generation and sum frequency generation, vanishes in optical fibers, owing to the inversion symmetry of silica glass. On the other hand, the third-order susceptibility plays the key role.

Major nonlinear effects in optical fibers include self-phase modulation (SPM), cross-phase modulation (XPM), four-wave mixing (FWM), stimulated Raman scattering (SRS), and stimulated Brillouin scattering (SBS). Next, we briefly discuss the basics of each of these effects.

2.9.1 Self-phase Modulation

SPM is the change in the phase of an intense optical pulse due to the nonlinear change of the refractive index of the material caused by this intense pulse. Such a self-induced phase shift can be written as (Litchinitser and Iakhnine 2011)

$$\phi_{\text{SPM}} = \gamma PL \tag{2.39}$$

where $\gamma = \frac{2\pi n_2}{\lambda A_{\text{eff}}}$ is the nonlinearity coefficient, n_2 is the nonlinear coefficient related to $\chi^{(3)}$, λ is the wavelength, A_{eff} is the effective core area, P is the peak power, L is the fiber length (assuming lossless case). The SPM results in a spectral broadening of a pulse, which may be disadvantageous for multichannel communication systems, which transmit signals at multiple wavelengths simultaneously. However, the SPM is extremely useful in many applications, including supercontinuum generation, optical regeneration, and soliton systems.

2.9.2 Cross-Phase Modulation

XPM is the nonlinear phase shift of an optical field at a given frequency (or a given polarization) induced by a co-propagating field at another frequency (or another

polarization). The effect of the XPM is twice as strong as that of the SPM as can be seen from the following expression (Litchinitser and Iakhnine 2011):

$$\phi_{\text{SPM+XPM}} = \gamma L\left(|E_1|^2 + 2|E_2|^2\right) \tag{2.40}$$

where the first term is responsible for the SPM, and the second one is due to the XPM. One of the major effects of the XPM is asymmetric spectral broadening. The XPM leads to many fundamental nonlinear phenomena such as soliton trapping and finds applications in Kerr shutters and intensity discriminators.

2.9.3 Four-Wave Mixing

FWM is a third-order parametric process that involves nonlinear interaction of four waves. In this process, two photons at frequencies ω_1 and ω_2 are annihilated and create two photons at frequencies ω_3 and ω_4, such that (Litchinitser and Iakhnine 2011)

$$\omega_3 + \omega_4 = \omega_1 + \omega_2 \tag{2.41}$$

The FWM process described by (2.41) relies on a phase-matching condition given by (Litchinitser and Iakhnine 2011)

$$\Delta k = k_3 + k_4 - k_1 - k_2 = 0 \tag{2.42}$$

Condition of (2.42) is easily satisfied in optical fibers for the partially degenerate case when $\omega_1 = \omega_2$. The FWM effect is used in many important fiber applications, including wavelength conversion, parametric amplification, and optical regeneration, among others.

2.9.4 Stimulated Raman Scattering

SRS is a process in which the incident photon is scattered by a molecule to a lower-frequency photon and is accompanied by a transition of the molecule between two vibrational states. The SRS can strongly affect the performance of multichannel transmission systems by transferring the energy between channels. At the same time, the SRS forms a basis of broadband Raman amplifiers and tunable Raman lasers that are of foremost importance for energy restoration in optical transmission systems and have numerous other applications as well (Litchinitser and Iakhnine 2011).

2.9.5 Stimulated Brillouin Scattering

SBS is a nonlinear process that originates from the interaction of light with acoustic phonons and results in generation of a backward-propagating Stokes wave downshifted in frequency from the pump wave. The SBS has a relatively low threshold (lower that for the SRS) and can be detrimental for fiber-optic transmission systems. However, the SBS finds applications in Brillouin lasers and amplifiers (Litchinitser and Iakhnine 2011).

2.10 Reliability Evaluation

The reliability of an integrated optical waveguide system indicates the probability that the system will be operational within acceptable limits for a given period of time. Advanced optical waveguides are very complicated systems. The dimensions of these structures are in the micrometer scale and getting smaller. Because of the fine features and large number of parts involved in each device, the probability of system failure is high unless high reliability of each device is ensured. In addition, some optical waveguides are being used in very harsh environments. For instance, under-the-hood applications in automobiles, missiles stored in desert sand, airplanes flying in high attitude where temperatures can drop below negative 60 °C, space stations exposed to strong radiation as well as extreme temperatures, etc. These hash environments have imposed stringent requirements on the reliability of integrated waveguide systems. The waveguide system must be designed to sustain high and low temperature extremes, to survive humid and corrosive surroundings, and to be protected from ultraviolet radiation. The mean time to failure for modern waveguide system may range from several days to several decades at room temperature. Reliability tests cannot be performed for such long durations, but can simulate the real situation based on well-designed, well-understood, and thoroughly implemented accelerated testing. Reliability testing and simulating can be used to determine which failure modes apply to a given part, how probable it is that these failure modes will occur while the part is in service, and how they might be prevented during the design and manufacture of this part. Therefore, identifying and understanding the mechanisms that cause component failure is the key to make a reliable waveguide system.

2.10.1 Failure Modes and Mechanisms

Reliability is defined as the probability that a component functions as designed, whereas failure indicates the probability that a component does not perform the

function any more. The photonic component failure model form can be expressed as (Naval 2008)

$$\lambda_P = \pi_Q(\lambda_{OB}\pi_{DCO}\pi_{TO}\pi_V + \lambda_{EB}\pi_{DCN}\pi_{TE}\pi_{RH} + \lambda_{TCB}\pi_{CR}\pi_{DT} + \lambda_{ind}) \tag{2.43}$$

where λ_P is predicted failure rate; π_Q is multiplier for quality; λ_{OB} is base failure rate from operational stresses; $\pi_{DCO} = \dfrac{DC}{DC_{10p}}$ is failure rate multiplier for duty cycle. $\pi_{TO} = e^{\left(\frac{-Ea_{op}}{.00008617}\left(\frac{1}{T_{AO}+T_R+273}-1/298\right)\right)}$ is factor for operating temperature. $\pi_V = \left(\frac{V_a+1}{V_c}\right)^{n_{vib}}$ is vibration factor; λ_{EB} is base failure rate from environmental stresses. $\pi_{DCN} = \frac{1-DC}{1-DC_{10p}}$; $\pi_{TE} = e^{\left(\frac{-Ea_{nonop}}{.00008617}\left(\frac{1}{T_{AE}+273}-1/298\right)\right)}$ is nonoperating temperature factor. $\pi_{RH} = \left(\frac{RH_a+1}{RH_c}\right)^{n_{RH}}$ is humidity factor; $\pi_{CR} = \frac{CR}{CR_1}$ is cycling rate factor; $\pi_{DT} = \left(\frac{T_{AO}+T_R-T_{AE}}{14}\right)^{n_{PC}}$ is delta temperature factor; and λ_{ind} is failure rate from induced stresses.

The model parameters are defined as follows:

λ_P is predicted failure rate, failure per million calendar hours
π_Q is failure rate multiplier for quality
λ_{OB} is base failure rate, operating
DC is duty cycle (fraction of calendar time in operation)
$DC_{10p} = 0.25$
π_{TO} is failure rate multiplier, temperature-operating
Ea_{op} is active energy-operating
T_{AO} is ambient operating temperature
T_R is the temperature rise above T_{AO}
π_V is failure rate multiplier, vibration level
V_a is Max vibration level applied (Grms)
$V_c = 1$
n_{vib} is vibration exponent
λ_{EB} is base failure rate, environment
π_{DCN} is failure multiplier, duty cycle-nonoperating
π_{TE} is failure rate multiplier, temperature-environment
Ea_{nonop} is activation energy, nonoperating
T_{AE} is ambient environmental temperature
π_{RH} is failure rate multiplier, relative humidity
RH_a is relative humidity (%)
$RH_c = 50$ %
n_{RH} is relative humidity exponent
λ_{TCB} is base failure rate, temperature cycling
π_{CR} is failure rate multiplier, cycling rate
CR = cycling rate (cycles per year)

$CR_1 = 1{,}000$
π_{DT} is failure rate multiplier, delta temperature
n_{PC} is temperature cycling exponent

By utilizing this model form, factors that account for the application and component-specific variables that affect reliability can be applied to appropriate additive failure rate term.

2.10.2 Reliability Qualifications

To ensure product reliability, extensive reliability tests need to be performed during product development and before a new product can be shipped. Commonly accepted accelerated tests include thermal cycling and thermal shock, steady state thermal soaking, mechanical vibration, voltage extremes and power cycling, high humidity and high pressure, and combination of the above.

2.10.2.1 Thermal Cycling and Thermal Shock

The single, dual, and triple chamber can be used for temperature cycling. In single chamber cycling, the load is placed in a stationary chamber, and is heated or cooled by introducing hot or cold air into the chamber. In dual chamber cycling, the load is placed on a moving platform that shuttles between stationary chambers maintained at fixed temperatures. In triple chamber temperature cycling, there are three chambers and the load is moved between them. This test is conducted to determine the ability of electronic packaging and thermal cooling system, including components and solder interconnects, to withstand mechanical stresses induced by alternating high and low temperature extremes. Permanent changes in electrical and/or physical characteristics can result from these mechanical stresses (JESD22-A104C). Typical testing conditions can be found from JESD22-A104C.

The thermal shock test is conducted to determine the resistance of a part to sudden exposure to extreme changes in temperature and to the effect of alternate exposures to these extremes. The conditions and recommended fluids can be found from JESD22-A106B.

Thermal cycling is an excellent test method for first order reliability assessment. However, it is not good for products with closely matched thermal coefficients of expansion because second-order effects, such as out-of-plane warpage, are not duplicated in this test method.

Comparability, power cycling or powered functional cycling is similar to thermal cycling, but more closely matches the actual service condition. It consists of a power-on transient in which the components go from room temperature to some steady state temperature in a matter of minutes. This steady state condition then lasts for several hours or longer before a power-off (cooling) transient occurs. The

power-off condition then lasts for several hours. The transient conditions are difficult to determine either experimentally or analytically. For this test, the same support structure should be modeled as closely as possible. The same environment conditions, such as cooling air flow, should be duplicated. With such care this approach will yield highly accurate reliability information. However, this method is more difficult, expensive, and time consuming.

2.10.2.2 Steady State Temperature–Humidity Bias Life Test

The steady state temperature–humidity bias life test is performed for the purpose of evaluating the reliability of non-hermetic packaged electronic devices in humid environments. It employs conditions of temperature, humidity, and bias which accelerate the penetration of moisture through the external protective material (encapsulant or seal) or along the interface between the external protective material and the metallic conductors which pass through it. The test requires a temperature–humidity test chamber capable of maintaining a specified temperature and relative humidity continuously, while providing electrical connections to the devices under test in a specified biasing configuration. Test conditions consist of a temperature, relative humidity, and duration used in conjunction with an electrical bias configuration specific to the device. The temperature of 85 $\pm$ 2 °C (dry bulb) and relative humidity of 85 $\pm$ 5 % should be applied to the entire useable test area. The wet bulb temperature is 81.0 °C, and vapor pressure is 49.1 kPa, and the duration of 1,000 (−24, +168) h applied continuously except during any interim readouts. The detail testing conditions can be found from EIA/JESD22-A101-B.

2.10.2.3 Mechanical Vibration

The vibration test is usually conducted in accordance with MIL-STD-167B. The vibration frequency is swept from 4 to 22 Hz. MIL-STD-167B requires an exploratory vibration test (10-min resonance survey sweep) a variable frequency test (5-min dwell at each frequency) and a 2-h endurance test at the resonant frequency.

Vibrating tables or shake tables are usually used to test electronic packaging and thermal cooling systems to determine or demonstrate their ability to withstand vibration. These machines are capable of producing three different types of vibration profile: sine sweep, random vibration, and synthesized shock. The part under test will typically be instrumented with one or more accelerometers to measure how the component responds to the vibration input. A sine sweep vibration profile, for instance, typically starts vibrating at low frequency and increases in frequency at a set rate (measured in hertz). The amplitude (measured in gs) of the sine wave may increase or decrease as well. A sine sweep is intended to look for resonant frequencies in the part. A random vibration profile will excite different frequencies along a spectrum at different times. Significant calculation goes into making sure that all frequencies get excited to within an acceptable tolerance band. A random

Table 2.5 Telecordia GR1209 required environmental and mechanical tests

Test	Condition
Temperature–humidity aging	85 °C/85 % RH for 14 days
Temperature–humidity cycling	−40 °C to 75 °C, 10–80 % RH, 42 cycles, 14 days
Water immersion	43 °C, pH 5.5, 7 days
Vibration	10–55 Hz, 1.52 mm, 2 h
Flex test	1 lb load, 100 cycles
Twist test	1 lb load, 10 cycles
Side pull	0.5–1 lb load, 90° angle, active
Cable retention	1.2–2.2 lb load for 1 month
Impact test	6 ft. drop, 8 cycles, 3 axes

Table 2.6 Telecordia GR1221 required environmental and mechanical tests

Test	Condition
High temperature storage (damp heat)	75 °C/90 % RH for 2,500 h
High temperature storage (dry heat)	85 °C, <40 % RH for 2,500 h
Low temperature storage	−40 °C, uncontrolled RH for 2,500 h
Temperature cycling	−40 to 75 °C, dwell $\geq$ 15 min, ramp @ 1 °C/min, 500 cycles
Temperature–humidity cycling	25 °C/uncontrolled RH to 75 °C/90 %, 4–16 h dwell, ramp @ 2 °C/min, 5 cycles
Thermal shock	T = 100 °C, dwell $\geq$ 30 min, transfer 2 min, 20 cycles
Salt spray	T = 35 °C, 5 % NaCl dissolved in 95 % H_2O, 168 h
Water immersion	43 °C, pH 5.5, 340 h

vibration test can be anything as short at 30 s up to several hours. It is intended to synthesize the effect of, for example, a car driving over rough terrain or a rocket taking off. A synthesized shock pulse is a short duration high level vibration calculated as a sum of many half-sine waves covering a range of frequencies. It is intended to simulate the effects of an impact or explosion. A shock pulse test typically lasts less than a second.

2.10.2.4 GR1209 and GR1221

Requirements for telecommunication network devices have been developed with the goal of assuring operation for 20–25 years. The major governing documents for passive optical components are two monographs from Telecordia, the GR1209 and GR1221 (Ma et al 2002). The Telecordia GR1209 focus primarily on optical performance tests and short-term reliability data (several weeks) that would apply to any manufactured lot of devices (Table 2.5, GR1209-1994). The Telecordia GR1221 is a document that focuses on comprehensive reliability assurance, in particular vendor and device qualification, lot-to-lot quality and reliability control, storage and handling (Table 2.6, GR1221-1994).

References

AA Sa (2013) Acousto-optic materials. http://www.acoustooptic.com/acousto-optic-material.html. Accessed 10 March 2013

Chien ST (2004) Waveguide fabrication using proton beam writing. PhD dissertation, National University of Singapore, Singapore

Christensen D et al (1992) Comparison of robust coupling techniques for planar waveguide immunosensors. Proc SPIE 1796:20–25

Dutton HJR (1998) Understand optical communications. IBM, Research Triangle Park

Edmund (2013) Understanding optical specifications. http://www.edmundoptics.com/technical-resources-center/optics/understanding-optical-specifications/?&pagenum=3. Accessed 26 Feb 2013

Elton NJ (2007) The complex refractive index and reflectometry versus ellipsometry. Reflectometry Technical Paper No. 3. http://www.Surfoptic.com. Accessed 1 Feb 2009

Gang SY (2005) Polymer based optical waveguides. Master's degree thesis, Universiti Teknologi Malaysia, Johor Bahru

Generic reliability assurance requirement for fiber branching components, Bellcore GR-1209-CORE, Bellcore, NJ, 1994

Generic reliability assurance requirements for fiber optic branching components, Bellcore GR-1221-CORE, Bellcore, NJ, 1994

Goering R, Rothhardt M (1986) Application of the refracted-near-field technique to multimode planar and channel waveguides in glass. J Opt Commun 7:82–85

Jung J et al (2004) Ellipsometry. Aalborg University, Aalborg

Kang ES, Lee TH, Bae BS (2002) Measurement of the thermo-optic coefficients in sol-gel derived inorganic-organic hybrid material films. Appl Phys Lett 81(8):1438–1440

Kaye & Laby (2012) Tables of physical & chemical constants. 2.5.11 Electro-optic materials. Kaye & Laby Online. Version 1.0. http://www.kayelaby.npl.co.uk/general_physics/2_5/2_5_11.html. Accessed 6 Dec 2012

Litchinitser N, Iakhnine V (2011) Optical waveguides: numerical modeling. http://optical-waveguides-modeling.net. Accessed 16 March 2012

Ma H et al (2002) Polymer-based optical waveguides: materials, processing, and devices. Adv Mater 14(19):1339–1365

MSU (2013) Acousto-optic effect. http://www.mt-berlin.com/frames_ao/descriptions/ao_effect.htm. Accessed 6 Feb 2013

Naval (2008) Photonic component and subsystem reliability process. Naval Air Systems Command Control Number: 08-1125

Park DH (2008) Characterization of linear electro-optic effect of poled organic thin films. PhD dissertation, University of Maryland, College Park

Scruby CB, Drain LE (1990) Laser ultrasonics: techniques and applications. Taylor & Francis, London

Tyszkieiwcz C et al (2005) Determination of the refractive index of the SE1211 resin using an SPR spectroscopy. Mol Quantum Acoust 26:267–271

Wu YC (2005) Planar waveguides of Y2O3, Y2O3:Tb3+ and YAG prepared by sol-gel: analysis, structure and optical. PhD dissertation, Claude Bernard University, Lyon

Yin L (2009) Study of nonlinear optical effects in silicon waveguides. PhD dissertation, University of Rochester, Rochester

http://www.springer.com/978-3-319-01549-1

Advanced Materials for Integrated Optical Waveguides

Tong, X.C.

2014, XXVII, 552 p. 124 illus. in color., Hardcover
ISBN: 978-3-319-01549-1